

FROST NUCLEATION AND GROWTH ON HYDROPHILIC, HYDROPHOBIC, AND
BIPHILIC SURFACES

by

ALEXANDER SCOTT VAN DYKE

BSME, Kansas State University, 2013
BSM, Kansas State University, 2013

A THESIS

submitted in partial fulfillment of the requirements for the degree

MASTER OF SCIENCE

Department of Mechanical and Nuclear Engineering
College of Engineering

KANSAS STATE UNIVERSITY
Manhattan, Kansas

2015

Approved by:

Major Professor
Amy Betz

Copyright

ALEXANDER SCOTT VAN DYKE

2015

Abstract

The purpose of this research was to test if biphilic surfaces mitigate frost and ice formation. Frost, which forms when humid air comes into contact with a surface that is below the dew point and freezing temperature of water, hinders engineering systems such as aeronautics, refrigeration systems, and wind turbines. Most previous research has investigated increasingly superhydrophobic materials to delay frost formation; however, these materials are dependent on fluctuating operating conditions and surface roughness. Therefore, the hypothesis for this research was that a biphilic surface would slow the frost formation process and create a less dense frost layer, and water vapor would preferentially condense on hydrophilic areas, thus controlling where nucleation initially occurs. Preferential nucleation can control the size, shape, and location of frost nucleation. To fabricate biphilic surfaces, a hydrophobic material was coated on a silicon wafer, and a pattern of hydrophobic material was removed using photolithography to reveal hydrophilic silicon-oxide. Circles were patterned at various pitches and diameters. The heat sink was comprised of two parts: a solid bottom half and a finned upper half. Half of the heat sink was placed inside a polyethylene base for insulation. Tests were conducted in quiescent air at room temperature, 22 °C, and two relative humidities, 30% and 60%. Substrate temperatures were held constant throughout all tests. All tests showed a trend that biphilic surfaces suppress freezing temperature more effectively than plain hydrophilic or hydrophobic surfaces; however, no difference between pattern orientation or size was noticed for maximum freezing temperature. However, the biphilic patterns did affect other aspects such as time to freezing and volume of water on the surface. These effects are from the patterns altering the nucleation and coalescence behavior of condensation.

Table of Contents

Nomenclature.....	v
List of Figures.....	vi
List of Tables.....	vii
Acknowledgements.....	viii
Chapter 1 - Introduction and Background.....	1
1.1 Microfluidics.....	1
1.2 Definitions.....	1
1.3 Motivation.....	1
1.4 Physics.....	4
1.5 Past Research: Increasingly Hydrophobic Surfaces.....	10
Chapter 2 - Fabrication and Design of Biphilic Surfaces.....	11
2.1 Teflon Deposition Technique.....	11
2.2 OTS Fabrication Process.....	12
Chapter 3 - Experimental Setup.....	16
Chapter 4 - Experiments: Frost Nucleation and Frost Growth.....	20
4.1 Glass Slides.....	20
4.2 Silicon Wafers.....	20
Chapter 5 - Results and Discussion.....	22
5.1 Results.....	22
5.2 Discussion.....	27
References.....	36

Nomenclature

A	=	Surface Area (m^2)
B	=	Molar Energy Density (kJ/mol)
CA	=	Contact Angle
ΔG	=	Gibbs Free Energy (J)
ΔG_{lat}	=	Latent Free Energy (J)
HNT	=	Heterogeneous Nucleation Theory
M	=	Molar Mass (g/mol)
P	=	Pressure (Pa)
R	=	Universal Gas Constant (J/mol·K)
RH	=	Relative Humidity (%)
S	=	Entropy (kJ/kg·K)
ST	=	Super Cooling Degree (K)
S_{sat}	=	Super Saturation
T	=	Temperature (K)
UV	=	Ultraviolet
V	=	Volume (m^3)
h	=	Enthalpy (kJ/kg)
r	=	Embryo Radius (m)

Greek Symbols

γ	=	Surface Tension (J/m ²)
θ	=	Contact Angle
ρ	=	Density (kg/m ³)
ω	=	Specific Humidity

Subscripts

STG	=	Solidification and tip growth
T	=	Temperature (K)
V	=	Vapor
c	=	Critical
conf	=	Configurational
crystal	=	Crystal
dew	=	Dew-point
e	=	Embryo
ex	=	Excess
liquid	=	Liquid
s	=	Surroundings
sat	=	Saturation
surface	=	Surface
w	=	Wall

List of Figures

Figure 1.1: Representation of different frost patterns that can form on fins based on surface treatment and operating conditions.	3
Figure 1.2: Water phase diagram [24].....	5
Figure 1.3: Temperature and convective heat transfer coefficient evolution through time during three steps of frost growth. All images are 1 mm x 1 mm [25]	6
Figure 1.4: Embryo geometry for (a) homogenous and (b) heterogeneous nucleation [2]	7
Figure 1.5: Variation of the contact angle factor [2] as generated in MATLAB	8
Figure 2.1: Typical micrographs (a) and (b) of surfaces with hydrophilic (black) and hydrophobic (gray) zones, respectively, and (c) bubbles that characteristically nucleate at the interface between areas of various wettability [40]	11
Figure 2.2: Manufacturing process for Teflon®-coated biphilic surface [42]	12
Figure 2.3: Biphilic surface geometries for (a) IL and (b) S arrangement. Gray dots represent hydrophilic areas, and the white background is hydrophobic.....	13
Figure 2.4: Manufacturing process of OTS-coated biphilic surface.....	15
Figure 3.1: (a) Experimental setup and (b) diagram of the test module	16
Figure 3.2: Solidworks drawing of the finned top plate of the heat sink	17
Figure 3.3: Solidworks exploded view of setup with bill of materials	18
Figure 3.4: (a) Top view of frost on a hydrophilic surface and (b) 3-D topographical map	19
Figure 4.1: Half-and-half slide showing difference in frost growth	20
Figure 5.1: Maximum freezing temperature for all surfaces with thermocouple uncertainty.....	23
Figure 5.2: Freezing on the 25IL surface at (a) 30%, (b) 60%, and (c) 75% RH.....	25
Figure 5.3: Nucleation and coalescence on the 25IL surface at 75% RH.....	27
Figure 5.4: Freezing droplets at (30%, 60%) RH for the (a, b) hydrophobic surface, (c, d) 200IL surface, (e, f) 200S surface, and (g, h) 25IL surface	29
Figure 5.5: (a) Pinning of water nucleation on the 25IL biphilic surface, (b) accumulation of nucleation at pattern interface, but no pinning on the 200S biphilic surface.....	34

List of Tables

Table 5.1: Freezing time data for 30% and 60% RH for all non-hydrophilic surfaces	23
Table 5.2: Average data for 60% RH frozen droplets for all non-hydrophilic surfaces	24

Acknowledgements

The research included in this thesis could not have been performed if not for the assistance, patience, and support of many individuals. I would like to extend my gratitude first and foremost to my thesis advisor Dr. Amy Betz for mentoring me over the course of my undergraduate and graduate studies.

I would also like to sincerely thank Dr. Steve Eckels for allowing us to use one of the rooms at the Institute for Environmental Research.

Finally, I would like to thank Diane Collard and Andres Martinez for their aid in experimentation.

This research was supported in part by the National Science Foundation under Grant No. 1448270.

Chapter 1 - Introduction and Background

1.1 Microfluidics

Microfluidics, a field of study earnestly developed in the late 1980s, currently remains in relative infancy [1]. Microfluidics explores phenomena and applications pertaining to fluid dynamics on scales small enough (a few micrometers to a few millimeters) to affect the balance of forces.

1.2 Definitions

The following definitions and terminologies are used frequently throughout this thesis:

- Biphilic surfaces have heterogeneous wettability that must be fabricated.
- A contact angle is the angle made at the interface between a liquid/vapor and a solid surface. This value quantifies a surface's wettability.
- Crystallography examines the arrangement of atoms in solids.
- Homogeneous nucleation occurs with pure water, void of any surrounding or internal foreign particles or surfaces.
- Heterogeneous nucleation occurs in the presence of foreign particles or nearby foreign surfaces. This type of nucleation was studied in the research for this thesis.
- Hydrophilic surfaces have a low surface energy and a water contact angle less than 90° .
- Hydrophobic surfaces have a high surface energy and a water contact angle greater than 90° .
- Ice Ih, the most common type of ice, was studied for the research for this thesis. Although at least 13 types of ice have been found and studied, other types besides Ice Ih occur at either very low temperatures (below -40°C) or pressures higher than atmospheric pressure.
- Nucleation refers to the localized appearance of water or ice on a surface in the form of condensation or desublimation.
- Optical microscopy requires a microscope to view the desired object. Optical microscopes use visible light and lenses for magnification.
- Superhydrophilic surfaces have a contact angle less than 5° .
- Superhydrophobic surfaces have a contact angle greater than 150° .

1.3 Motivation

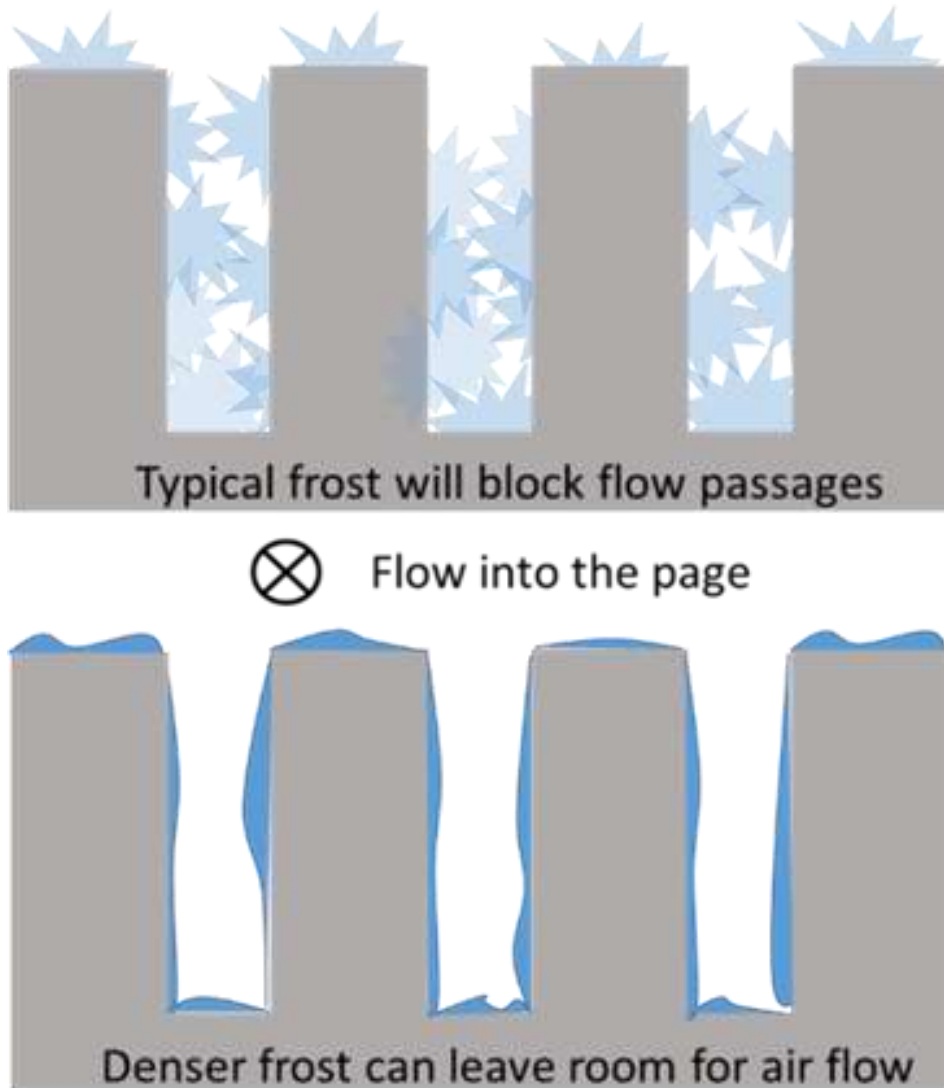
Frost forms when humid air comes into contact with a solid surface at a temperature below the dew point and freezing temperature of water. A fundamental understanding of frost formation and creation of robust frost-mitigating surfaces can help save energy by increasing refrigeration

system efficiencies [2], [3] and improving power transmission [4]. These surfaces can also improve aircraft safety by preventing ice formation on the wings of airplanes [5]. Over a fifteen year period, 20 of 74 control loss airplane crashes were due to icing [6]. Additionally, the Environmental Protection Agency estimates that deicing cost US airports approximately \$500,000,000 each year. Previous research has primarily focused on increasingly hydrophobic surfaces that have been proven to slow condensation as well as ice and frost formation [2], [7]. Superhydrophobic surfaces can decrease the temperature required for frost formation and increase required freezing time [5], 8-15]. However, these effects are highly sensitive to fluctuating operating conditions [4] and surface roughness or feature size [5], [10].

Additionally, there are circumstances where frost formation cannot be prevented due to the operating conditions. For example, air source heat pump systems are used for heating and cooling of residential and commercial buildings all year around. They are energy efficient, compact, and have low installation costs. An air source heat pump exchanges heat directly from the indoor environment to the outdoor ambient air, and during winter operation, the outdoor coil might accumulate frost on its surface. Frost forms on the surface of the outdoor coils when humid air comes in contact with the coil surface which has a temperature below the dew point temperature of entering air and also below freezing point of water (0 °C). Frost, on the surface, acts as an insulator and air passage blocker, see Figure 1.1, reducing the heat transfer rate and increasing the air pressure drop of air passing through the coil. Defrost cycles are periodically executed in between the heating times to melt the ice, drain the water from the outdoor coil, and free its surface from accumulated frost before the heating service could start again. Microchannel coils have been employed recently in heat pump applications to replace conventional fin and tube coils due to their compactness, lower coil weight and less refrigerant charge which could lower the direct contribution to global warming due to potential refrigerant leakage [5, 14-16]. These heat exchangers are usually made of Aluminum and because of the low conductive thermal resistance of the microchannel tubes, the fin base temperature is closer to the local saturation temperature of the refrigerant in comparison to conventional fin and tube type heat exchangers. While in cooling mode microchannel heat exchangers increase the energy efficiency compared to spine fin or plate fin-and-tube coils with similar face area, during heating mode the energy performance of heat pump systems with microchannel outdoor coils are generally low due to a

higher frequency of defrost cycles [16, 17]. Because frequent defrost cycles penalize the heating seasonal energy efficiency, it is crucial to understand the characteristics of frost growth on outdoor coils and develop heat exchangers that would minimize, if not eliminate, defrost cycles. There are several parameters that affect frost formation on outdoor coils, such as air velocity, air humidity, air temperature, cold surface temperature, [18, 19] surface energy, fin-base surface microscopic characteristics (include coatings and roughness or brazing fluxes) [20, 21], fin geometry, and coil water retention after defrost cycles [22].

Figure 1.1: Representation of different frost patterns that can form on fins based on surface treatment and operating conditions.

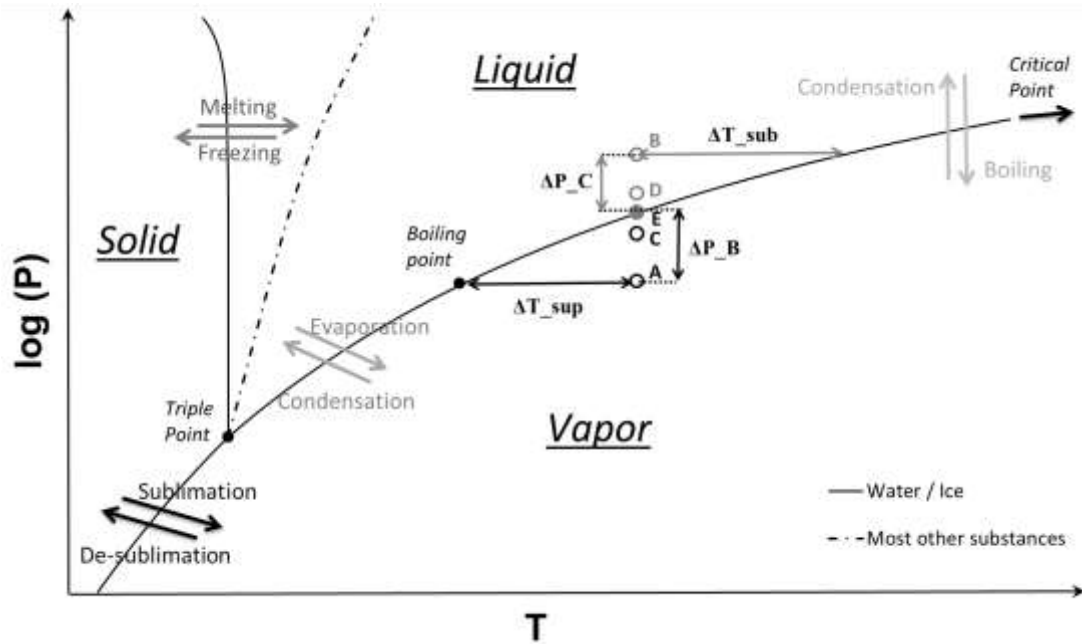


N. H. Fletcher [11] states that “ice has a random orientation of molecular dipoles and a substrate which imposes any ordering on these will reduce the entropy of the ice molecules in the embryo and so increase its free energy.” The hypothesis of this research was that biphilic surfaces would control aspects of frost formation, e.g. surface water coverage, volume of water, freezing time, and the suppression of maximum freezing temperature. Superhydrophobic surfaces currently apply increased ordering to the system, but the biphilic surface is not uniform like a superhydrophobic surface. Hydrophilic areas of the surface provide a preferential area for condensation to nucleate, thereby increasing the ordering of the ice and the free energy barrier. The ultimate goal of these surfaces is frost manipulation. However, circumstances may arise that require various levels of frost growth, such as complete ice prevention on aircrafts or a desirably dense frost layer to lessen the heat transfer effect in applications such as refrigeration.

1.4 Physics

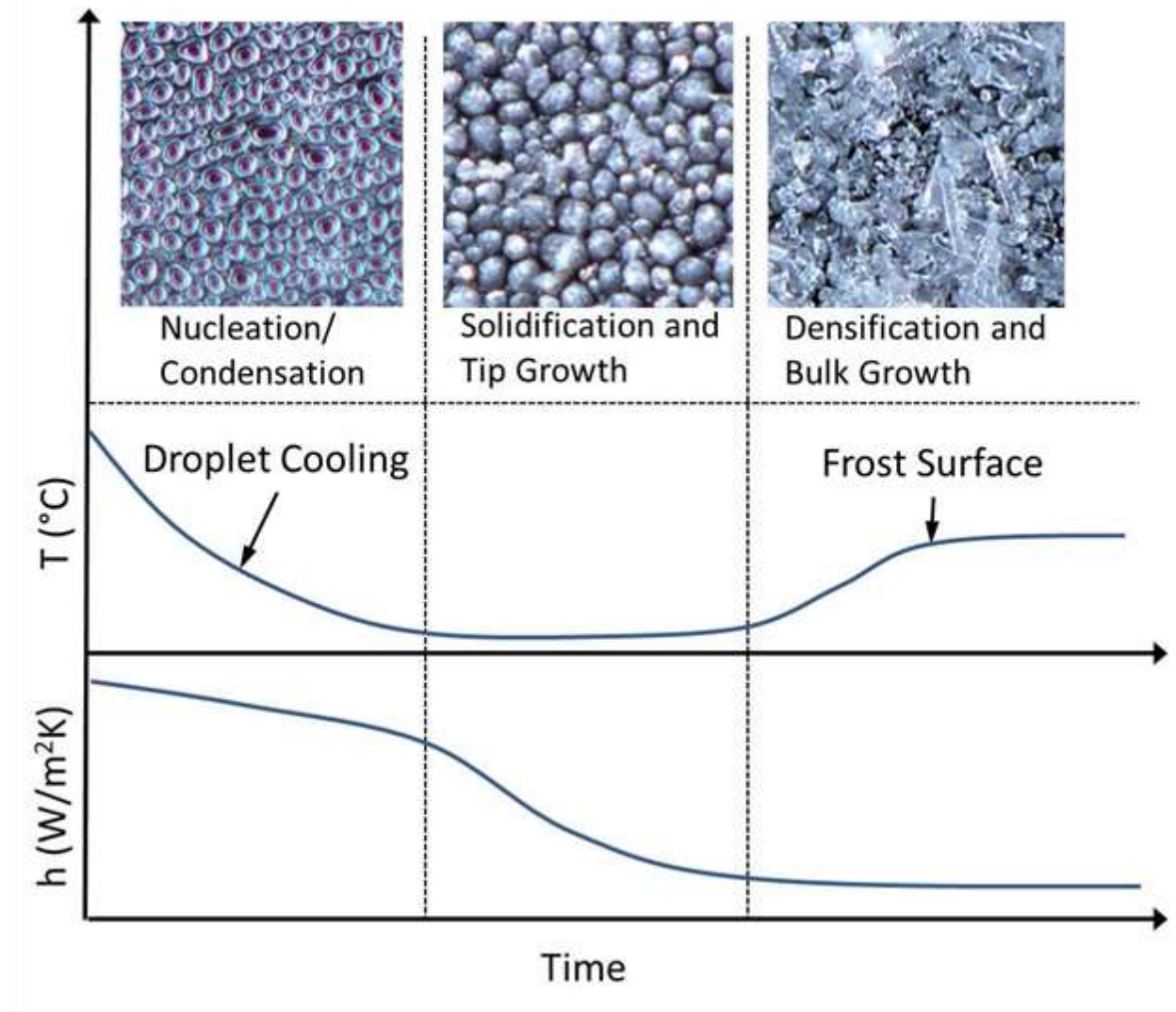
Frost has two methods of formation: desublimation and condensation freezing on a surface. Deposition occurs when the system pressure is below the triple point of water, and condensation occurs when the system pressure is above the triple point, as shown in Figure 1.2 [24].

Figure 1.2: Water phase diagram [24]



The frost growth process involves three steps: nucleation/condensation, solidification and tip growth (STG), and densification and bulk growth (DBG). These three steps are associated with corresponding temperature and heat transfer coefficient curves, as shown in Figure 1.3.

Figure 1.3: Temperature and convective heat transfer coefficient evolution through time during three steps of frost growth. All images are 1 mm x 1 mm [25]



Frost is formed by a heterogeneous water vapor nucleation process. The Gibbs energy barrier must be overcome in order to initiate phase change of the embryo from a saturated to a supersaturated state. The Gibbs free energy and latent free energy can be expressed as

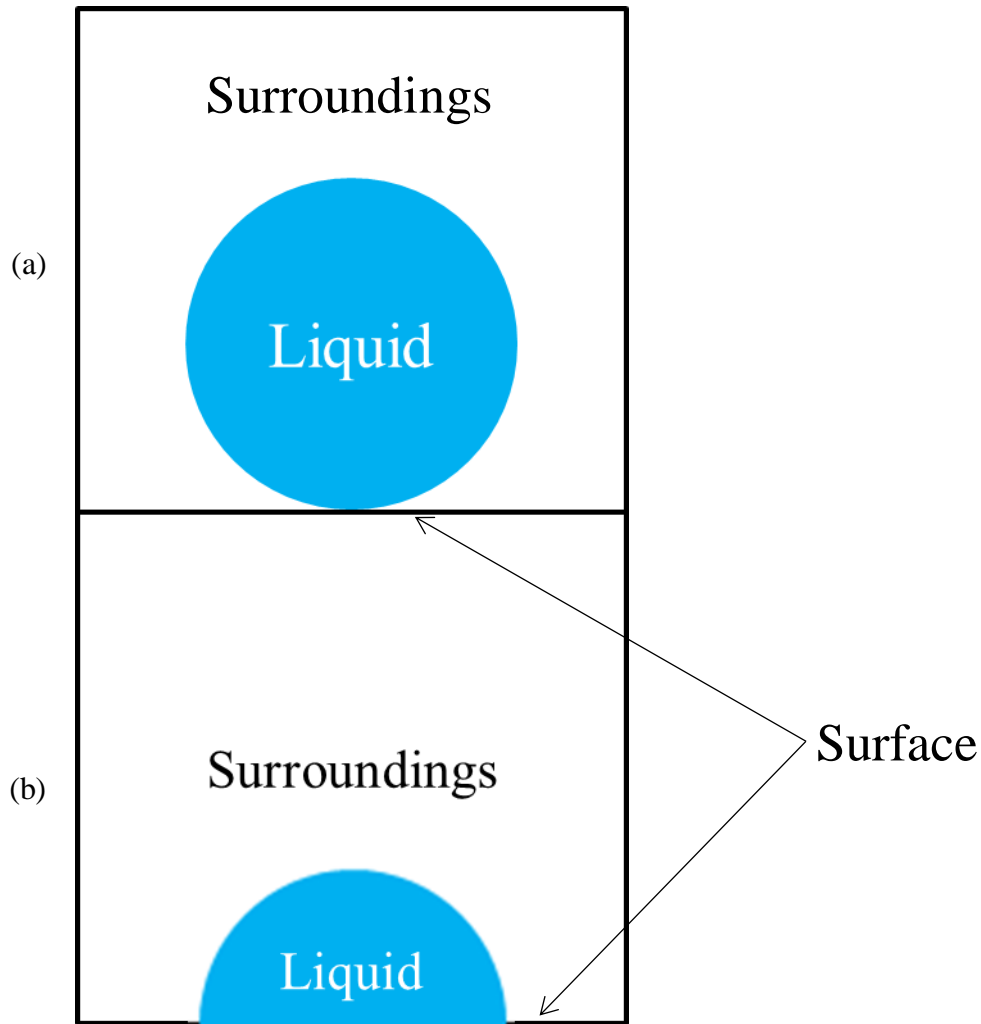
$$\Delta G = \Delta G_{lat} + A_{se}\gamma_{se} - A_{sw}(\gamma_{sw} - \gamma_{ew}) \quad (1)$$

$$\Delta G_{lat} = \frac{\rho VRT}{M} \ln\left(\frac{\omega_{air}}{\omega_e}\right) \quad (2)$$

where ρ , V , M , and T are embryo density, volume, mass, and temperature, respectively. R is the universal gas constant and ω_{air} and ω_e are the humidity ratio or specific humidity of the surrounding air and the embryo surface. Equation 1 can be modified to account for a semispherical embryo in which the contact angle determines the shape. A critical embryo radius

that maximizes energy required to initiate nucleation exists on a surface with a constant contact angle [2], as shown in Figure 1.4.

Figure 1.4: Embryo geometry for (a) homogenous and (b) heterogeneous nucleation [2]



In Figure 1.4, γ represents surface tension of the various interfaces and A represents surface areas. The interfaces are embryo-wall, surroundings-wall, and surroundings-embryo. Substituting latent free energy (1) and the identities listed in Equations (3) - (7) into the Gibbs free energy Equation (2) yielded the form of required energy for nucleation, as presented in Equation (8):

$$\theta = \cos^{-1}(\gamma_{sw} - \gamma_{ew})/\gamma_{se} \quad (3)$$

$$V = \pi h^2(3r - h)/3 \quad (4)$$

$$A_{se} = 2\pi r h \quad (5)$$

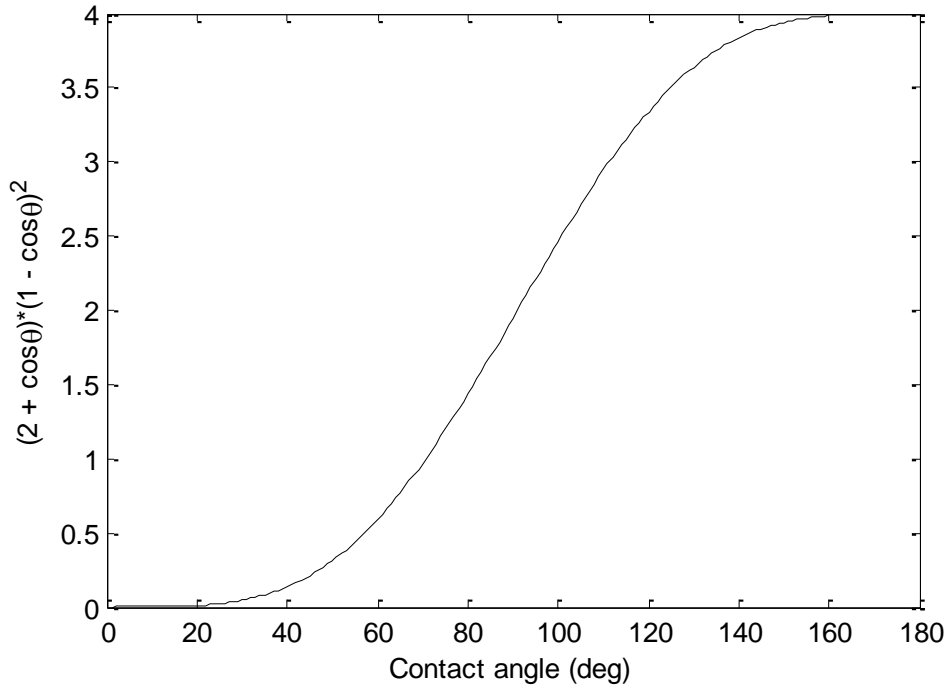
$$A_{ew} = \pi r^2 \sin^2 \theta \quad (6)$$

$$h = r(1 - \cos \theta) \quad (7)$$

$$\Delta G = \left[-\frac{\pi}{3} r^3 \frac{\rho RT}{M} \ln \left(\frac{\omega_s}{\omega_{sat,e}} \right) + \gamma_{se} \pi r^2 \right] (1 - \cos \theta)^2 (2 + \cos \theta) \quad (8)$$

Therefore, energy required for nucleation is directly dependent on the contact angle of the surface, as shown in Figure 1.5.

Figure 1.5: Variation of the contact angle factor [2] as generated in MATLAB



We can find a critical embryo size by taking the derivative of ΔG with respect to the radius of the embryo and setting this value to zero:

$$r_c = 2\gamma_{se} \left[\frac{\rho RT}{M} \ln \left(\frac{\omega_s}{\omega_{sat,e}} \right) \right]^{-1} \quad (9)$$

Substituting the critical radius into (8) yields the critical Gibbs free energy

$$\Delta G_c = \frac{4\pi}{3} \frac{\gamma_{se}^3}{\left[\frac{\rho RT}{M} \ln \left(\frac{\omega_{sat,e}}{\omega_s} \right) \right]^2} (1 - \cos \theta)^2 (2 + \cos \theta), \quad (10)$$

thereby exhibiting dependency on the contact angle, specific humidity, and surface energy at the interface of the surroundings and the embryo.

Becker and Doring's [26] model approximated the embryo formation rate, I , based on the kinetic constant, $I_0=10^{25}$ embryos/cm², the Boltzmann constant, $k=1.381 \cdot 10^{-23}$ J/K, and the surface temperature in Kelvin:

$$I = I_0 \exp\left(\frac{\Delta G_c}{kT_w}\right). \quad (11)$$

Na and Webb [20], Jung et al. [10], and Piucco et al. [2] showed that supercooling and supersaturation occur at the cryosurface during frost formation. These factors can be measured by Equations (12) and (13):

$$S_T = T_{surface} - T_{dew} \quad (12)$$

$$S_{sat} = \frac{P_V - P_{V,sat}}{P_{V,sat}} \quad (13)$$

Piucco et al. [2] developed a model that closely predicts the onset of nucleation based on contact angle and supercooling degree. The determination was made that any supercooling degree greater than 5 °C guaranteed nucleation, no matter the contact angle. Also, contact angles above 140 degrees had no effect on the supercooling degree.

Hayashi et al. [27] observed and classified nine frost classes into four types (A, B, C, and D). These types were based off the ΔC - t_s plane which shows that concentration difference between the main stream and the cryosurface, and the cryosurface temperature are the two main parameters. Hayashi et al.'s finding agrees with standard crystallography, and, in their work, concentration is specific humidity (kg/kg). They observed that less supercooling and less supersaturation led to denser frost because of lower linear growth rate and lower surface roughness of the frost. Changes in frost density with various parameters were also investigated. With time as a dependent variable, the increase of frost density was approximately parabolic. Compared to non-dimensional frost height (L/\bar{L}), relative comparison is clearer between the four types of frost formation. Density of type D changed less than the other types, while densities of A and B changed greatly. Finally, they investigated thermal conductivity of frost layers, and they calculated effective conductivity of the porous frost layer from instantaneously measured values of frost height, heat flux, frost surface temperature, and cryosurface temperature, assuming that the temperature profile was linear across the frost layer. Other researchers have found that thermal conductivity through a frost layer is dependent upon the frost structure, internal diffusion

of water vapor, and the eddy generated by frost surface roughness. They formulated a mathematical model to determine effective thermal conductivity through the frost layer.

1.5 Past Research: Increasingly Hydrophobic Surfaces

Hydrophobic and superhydrophobic coatings have been widely investigated for their frost mitigating potential [5, 9-10, 12-16, 28-29]. However, superhydrophobic surface may actually increase frost formation due to the increased surface area and available nucleation sites [5, 10] and their effect on frost density is unknown. Jung et al. [10] proposed a modification to classical heterogeneous nucleation theory. Their study results showed that freezing time delays depend on two competing parameters: roughness and contact angle. They found that, in agreement with other sources, the superhydrophobic surface delayed freezing times, but they found that extremely smooth, hydrophilic surfaces also delayed freezing time. In fact, the tested silicon wafer delayed freezing time approximately 850 seconds, more than 10 times longer than the superhydrophobic polyvinylidene fluoride (PVDF) ($\theta \approx 145^\circ$) sample. According to classical heterogeneous nucleation theory, a 90° contact angle would produce a large freezing time delay. Therefore, Jung et al. modified the model. To account for the difference in freezing time delay, Jung et al. investigated the reduced disorder of water molecules near a surface (compared to “bulk liquid”) that carried a decrease in excess entropy, meaning that the viscosity changed according to the relationship in

$$\eta = \eta_0 \exp\left(\frac{A}{TS_{conf}}\right) \quad (14)$$

where $A=31.9$ kJ/mol and $\eta_0=1.64 \times 10^{-5}$ Pa*s. Configuration entropy can be estimated as $S_{conf} \approx S_{ex} = S_{liquid} - S_{crystal}$. Their trends are in agreement with their data, but uncertainties such as hydration layer thickness, hydrodynamic properties, and quantitative atomic-scale information are related to this modification. This finding agrees well with Na and Webb’s 2004 [20] paper in which they proved that air is supersaturated, or more ordered, at the cryosurface. There has also been much research into the effects of structures on frost formation [30-41].

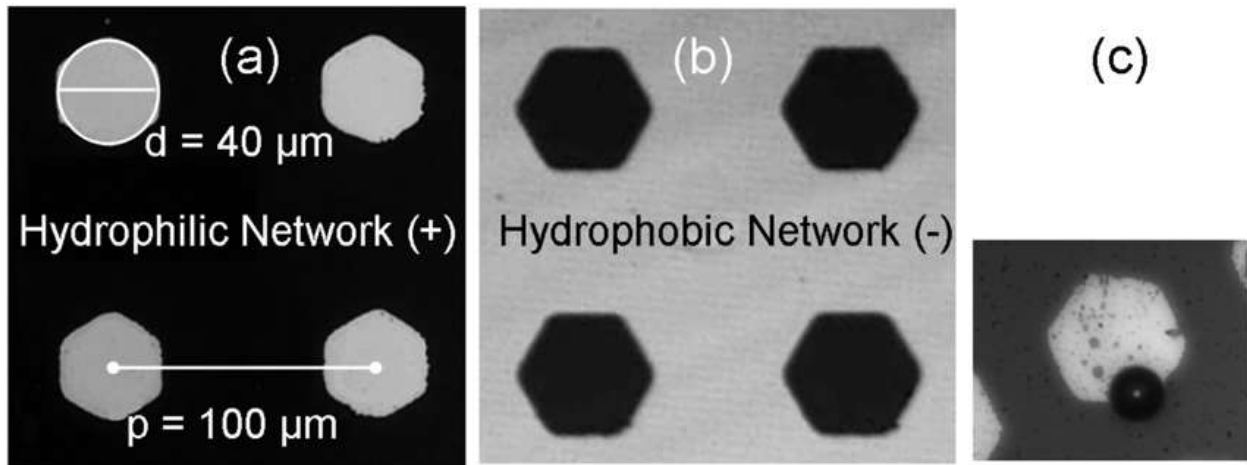
Chapter 2 - Fabrication and Design of Biphilic Surfaces

Modification of surfaces' physical and chemical properties, such as surface energy, wetting properties, roughness, and available surface area, has been an area of great interest in microfluidic systems research. Dr. Amy Betz [42] and her sponsoring professor at Columbia University, New York City, NY, Dr. Daniel Attinger, proposed biphilic surfaces as a means of surface enhancement for pool boiling. Dr. Betz suspected biphilic surfaces could also be translated into frost formation because the theory for heat transfer enhancement is similar, but in the opposite direction of heat transfer.

2.1 Teflon Deposition Technique

At Columbia University, Dr. Betz and Dr. Attinger worked with hexagonal biphilic surfaces that used Teflon® as the hydrophobic material, as shown in Figure 2.1.

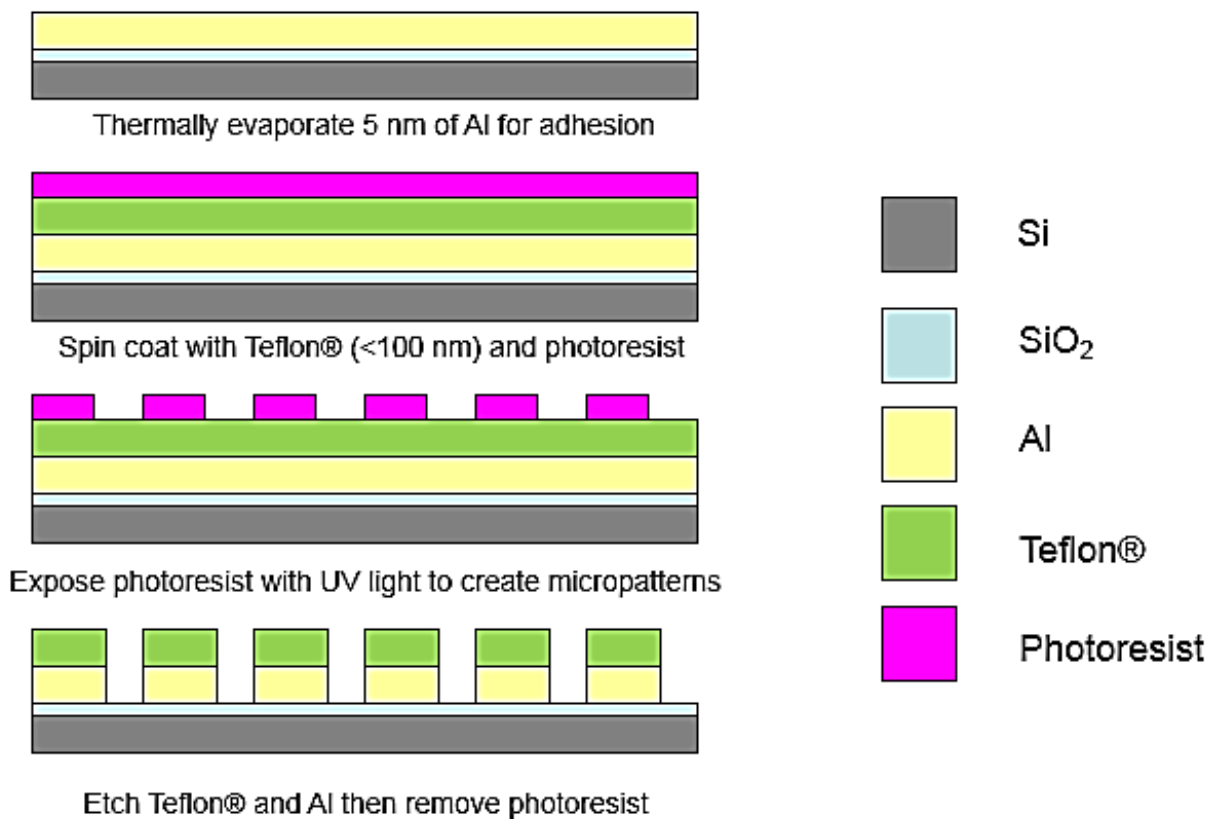
Figure 2.1: Typical micrographs (a) and (b) of surfaces with hydrophilic (black) and hydrophobic (gray) zones, respectively, and (c) bubbles that characteristically nucleate at the interface between areas of various wettability [40]



In order to fabricate the hexagonal biphilic surfaces, the oxidized, two-sided polished silicon wafer was coated with a 25 nm aluminum layer. An approximately 100 nm thin hydrophobic coating of Teflon® (AF400, DuPont) diluted in Fluorinert (FC-40) at a ratio of 1:3 was then spun onto the top of the aluminum layer. The wafer was baked at 90 °C for 20 minutes, and then a 1 μm layer of positive photoresist (S1818, Shipley) was spun atop the Teflon®. The wafer was exposed to 180 mJ/cm^2 of ultraviolet (UV) light using a transparency mask. The exposed area of

photoresist, Teflon, and aluminum were then removed using oxygen plasma and a developer (300 MIF, AX Electronic Material). The remaining photoresist was removed with acetone. Figure 2.2 shows a diagram of the process.

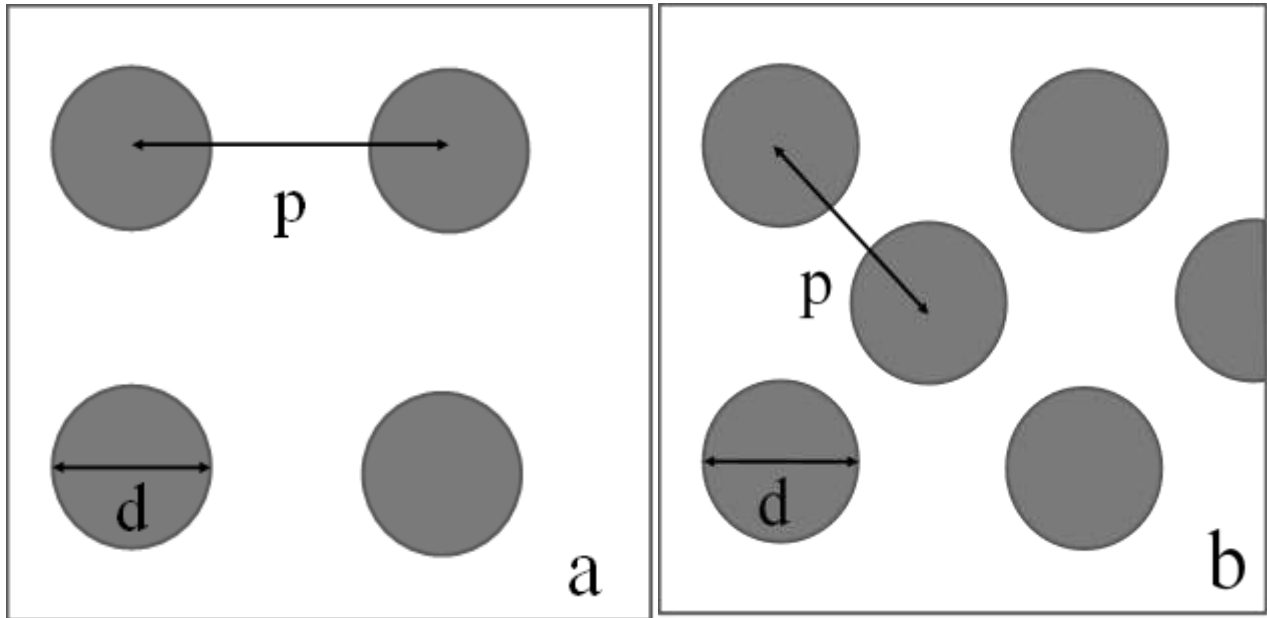
Figure 2.2: Manufacturing process for Teflon®-coated biphilic surface [42]



2.2 OTS Fabrication Process

Fabricated surfaces used in the current study differed in design from Dr. Betz's surfaces. Surface patterns used in this study, shown in Figure 2.3, were circular, hydrophilic areas with a hydrophobic background. The two patterns were in-line (IL) and staggered (S).

Figure 2.3: Biphilic surface geometries for (a) IL and (b) S arrangement. Gray dots represent hydrophilic areas, and the white background is hydrophobic



These circular patterns varied from 25-200 μm in diameter and had pitches of 0° and 60° . For each pattern, the pitch-to-diameter ratio is 2.

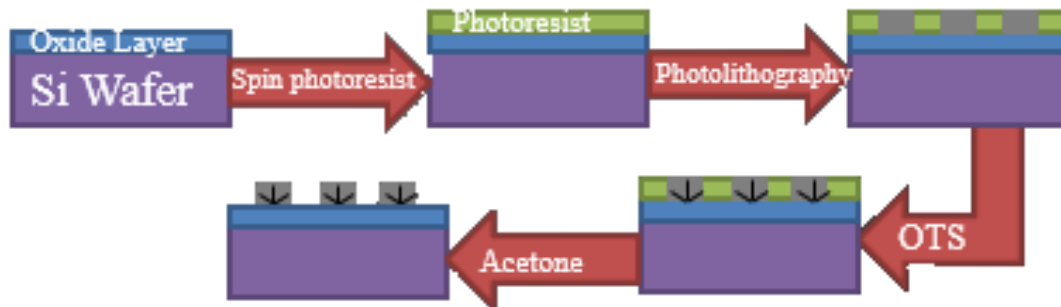
The Class 1000 clean room in Ward Hall, part of Dr. Douglas McGregor's SMART (Semiconductor Materials Academic Research and Teaching) Lab at Kansas State University, Manhattan, KS, was used to fabricate the mixed surfaces. A majority of projects in the SMART Lab relate to semiconductors, but research involving gas-filled detectors, radiation measurements, scintillation detecting materials, and neutron activation analysis is also conducted in the Lab. Equipment used in the Class 1000 clean room included a Karl Suss MJB3 Scanning IR Mask Aligner, a Laurell Photoresist Spinner, a Leitz Ergolux Inspection Microscope, and an LFE Plasma Asher.

The fabrication process was initiated by cleaning the silicon wafers in the LFE Plasma Asher. These wafers were a product of International Wafer Service, an incorporation that specializes in silicon wafer production. The wafers used in this study were 3 in. in diameter, 200-300 nm thick, and $\langle 111 \rangle$ orientation with a 2000\AA thick thermal oxide layer. To use the Plasma Asher, a vacuum was turned on from inside the room and oxygen was supplied to the asher from a tank. A maximum of three wafers were placed in a wafer rack (to ensure sufficient cleaning) located in

the asher; the door was closed and vacuum-sealed. The cleaning process, which took 30 min, removed all foreign particles from the silicon wafer surfaces. After cleaning, each wafer was placed into the Laurell Photoresist Spinner, a nickel-sized drop of Sigma Aldrich S1816 Positive Photoresist was administered to the wafer surface, and it was spun at 800 rpm for 10 sec and then 3600 rpm for 30 sec. Throughout the spinning process, the surface was vacuumed to the spinner and nitrogen flowed in the top of the spinner to prevent photoresist from splattering back onto the surface when it spun off of the surface. Spinning the photoresist created a thin layer of photoresist on the silicon wafer. After the spin was completed, the wafer was prebaked on a hot plate at 115 °C for 1 min, consequently enhancing crosslinking of the photoresist to increase the photoresist adherence strength. The wafer was then placed in the Karl Suss MJB3 Scanning IR Mask Aligner for exposure to UV light. A patterned mask was present between the UV light and the surface, creating the surface pattern. Only clear areas of the positive mask were exposed to the light, thereby breaking down the photoresist. Humidity and room temperature significantly affected the exposure time in such a way that a consistent exposure time was never reached, falling between 5 sec and 10 sec. After exposure, the silicon wafer was placed in a bath of MF CD-26 developer. The developing process removed the exposed photoresist, leaving behind photoresist in the pattern of the mask. After the exposed photoresist was removed, the wafer was placed into a deionized water bath to terminate the developing process.

After processing in the SMART Lab, the surfaces were returned to the Multiphase and Microfluidics Lab at Kansas State University, where they were made biphilic. The silicon wafers were placed in a bath of a 1% hydrophobic octadecyl(trichloro)silane (OTS) to Toluene mixture for 15 min, thereby coating a self-assembled monolayer (SAM) of OTS on the silicon wafers. Immediately following the coating, the wafers were placed in a bath of chloroform for 20 min to remove any OTS that did not adhere to the surface. Finally, the surfaces were bathed in acetone to remove any lingering OTS and remove the photoresist, revealing the hydrophilic silicon-oxide underneath the photoresist in the desired pattern. Isopropanol and deionized water were used to clean the completed biphilic surfaces before every test to ensure accurate surface tension without organic contaminants. The entire process is depicted in Figure 2.4.

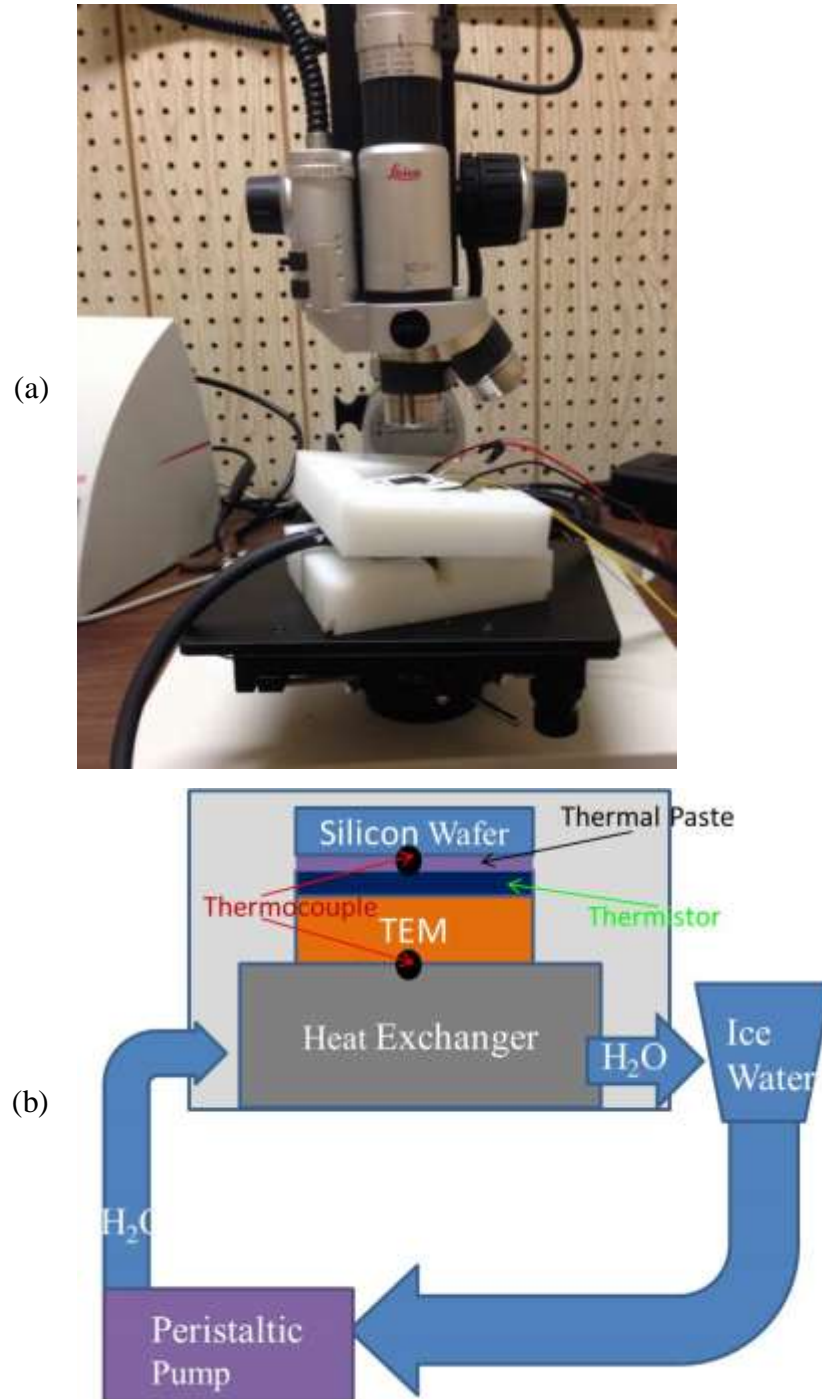
Figure 2.4: Manufacturing process of OTS-coated biphilic surface



Chapter 3 - Experimental Setup

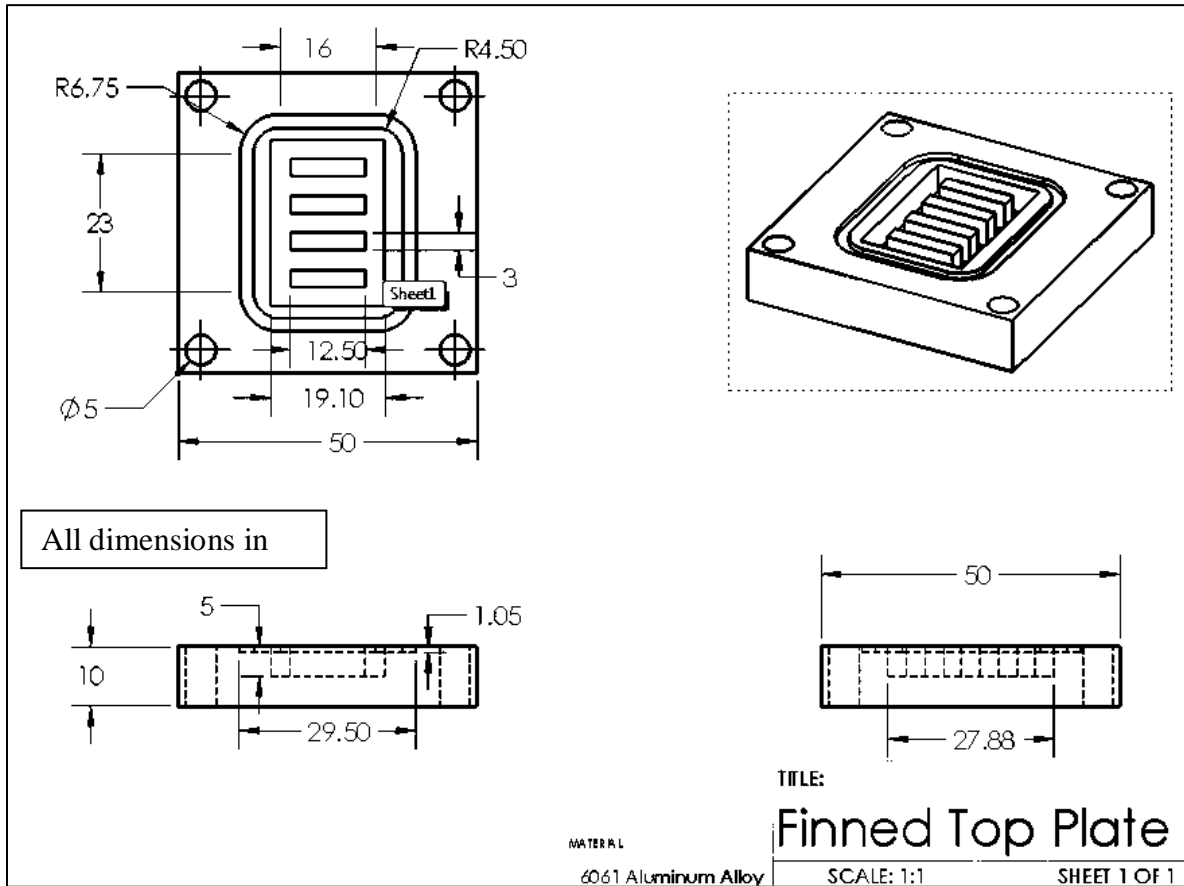
The surfaces were tested using a test setup shown in Figure 3.1.

Figure 3.1: (a) Experimental setup and (b) diagram of the test module



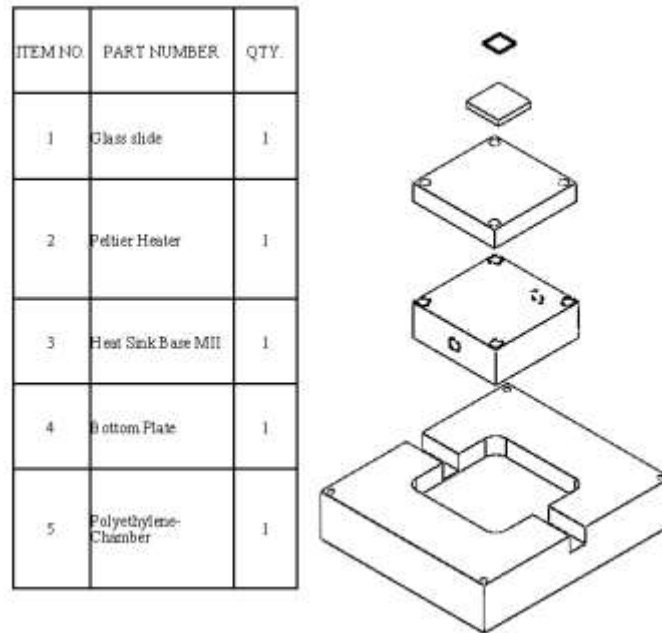
The microscope shown is 2 ft tall. The base of the test module was polyethylene and the heat sink was aluminum, comprised of a solid bottom half, and a finned top half. Figure 3.2 illustrates the heat sink and its dimensions, and Figure 3.3 presents an exploded setup view.

Figure 3.2: Solidworks drawing of the finned top plate of the heat sink



Half of the heat sink sat inside the polyethylene for insulation. A peristaltic pump pumped ice water through the heat sink, and a Peltier cooler was placed atop the heat sink to lower the surface temperatures to a range of -20 °C to -5 °C.

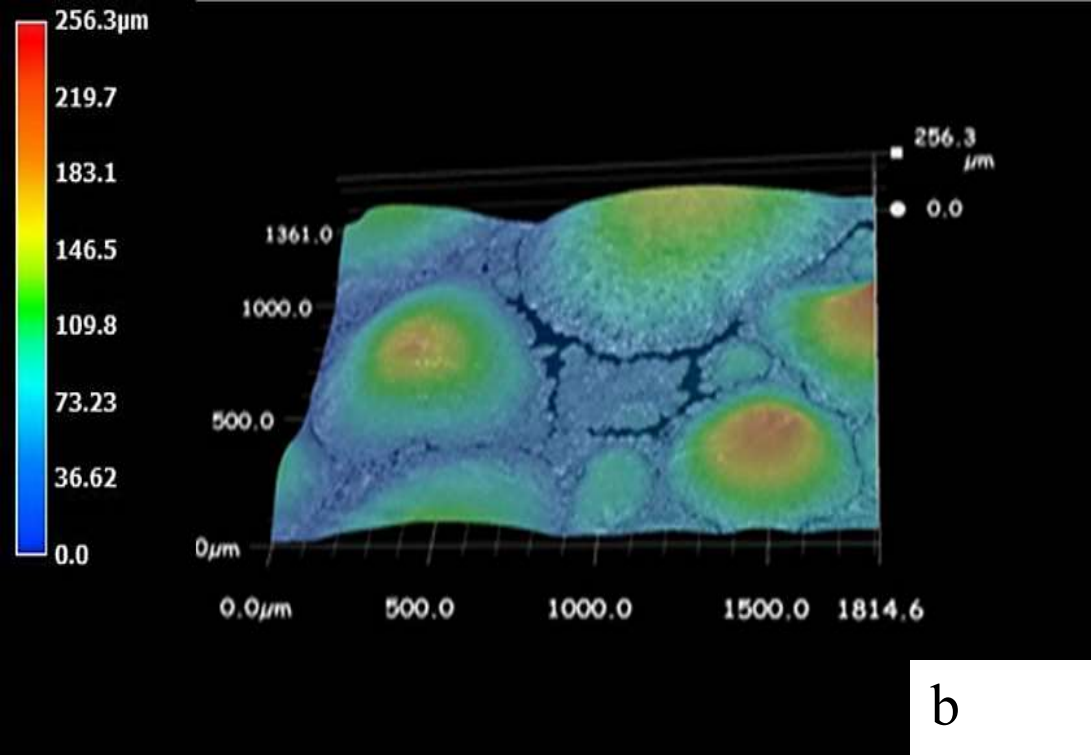
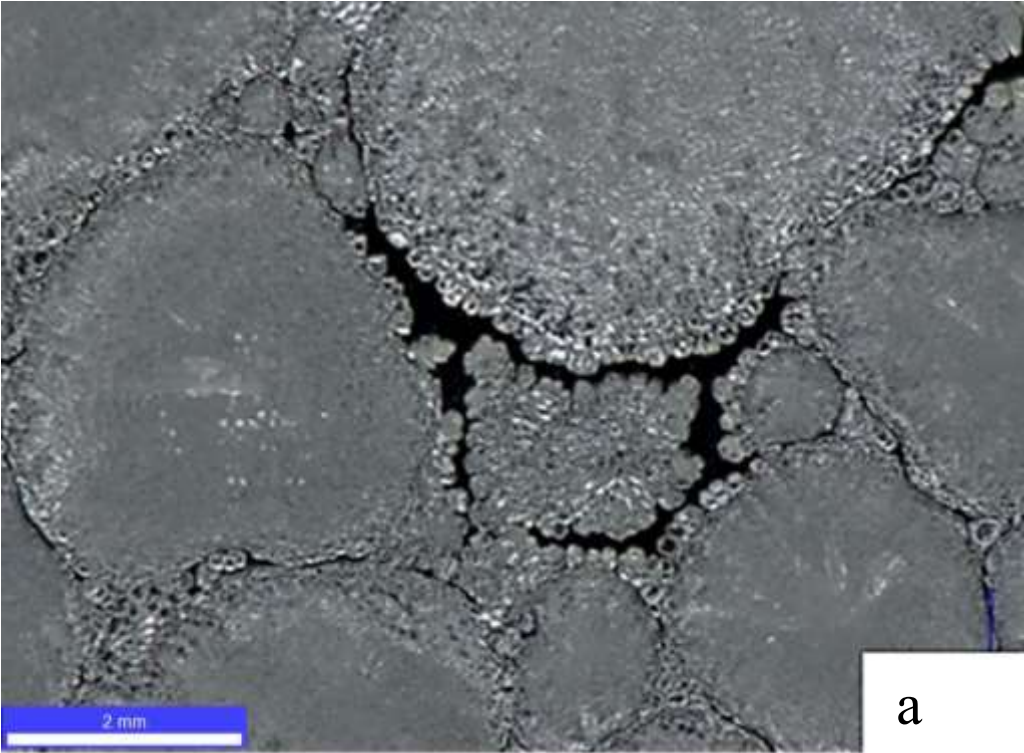
Figure 3.3: Solidworks exploded view of setup with bill of materials



Thermal paste was used to ensure sufficient thermal contact between a slide and the cooler. Temperature readings were taken with a Type K thermocouple through an NI 9211 DAQ with an NI cDAQ-9174 chassis and processed with NI LabVIEW with a ± 0.5 °C uncertainty. A LabVIEW VI was developed to control power flowing to the Peltier cooler in order to control the desired temperature. The signal to the power supply was sent through an RS232 serial cable. An Omega RHXL-3SD thermometer-hygrometer was used to measure relative humidity (RH) with $\pm 3\%$ RH uncertainty.

A Leica DVM2500 microscope was used to record videos and take images of the experiments. Depth of frost was found using the Montage application of the Leica DVM2500 that stepped through focuses with one micron resolution and pieced together a top-to-bottom in-focus image. Then the Leica Maps program produced a 3-D image for analysis. Figure 3.4 shows a 3-D image of (a) frost and a (b) topographical map.

Figure 3.4: (a) Top view of frost on a hydrophilic surface and (b) 3-D topographical map

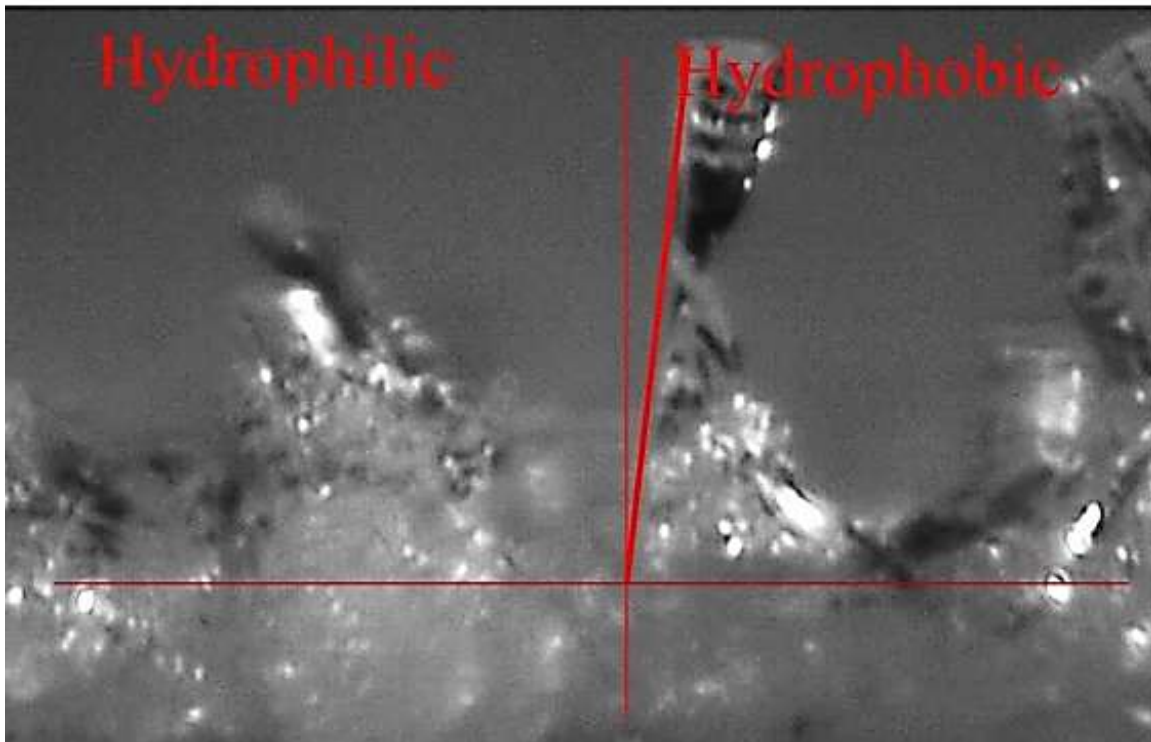


Chapter 4 - Experiments: Frost Nucleation and Frost Growth

4.1 Glass Slides

For this study, testing initially began on hydrophilic glass surfaces. The decision was made to switch to silicon wafers because they have a much higher thermal conductivity, thereby simplifying the process of reducing the temperature of the silicon. Tests were also initially taken with an optical camera (ThorLabs) with a 7x zoom lens attached to a 2x TV tube (Edmund Optics VIS Lenses). Data taken from these initial tests were not valid because of the camera's lack of precision and definition. Results from these tests revealed that one surface fabricated and tested on a glass slide was half hydrophilic glass and half hydrophobic OTS. Frost growth on the surface yielded the image in Figure 4.1, which shows a clear division between frost formations on the two sections. Figure 4.1 is approximately 1 mm wide x 0.65 mm high.

Figure 4.1: Half-and-half slide showing difference in frost growth



4.2 Silicon Wafers

After attempting to test with the above optical camera equipment and failing to collect data of acceptable quality, the decision was made to switch to silicon wafers because they have a

much higher thermal conductivity, so it would be easier to reduce the temperature of the silicon. High-powered optical microscopes were researched, resulting in the purchase of a Leica DVM2500 with the following features that allow collection of high quality data:

- Maximum of 2500X zoom
- Tilting microscope
- Image measurement analysis
- Video in HD
- In-image scale bar

Another testing change involved a move to an environmentally controlled room at the Institute for Environmental Research (IER) in which chambers are temperature and humidity controlled. Finally, a temperature controller was utilized instead of a constant power input to the Peltier cooler.

Chapter 5 - Results and Discussion

5.1 Results

Three of the initial nine biphilic patterns were fabricated and tested. Tests were also conducted on plain hydrophilic and plain hydrophobic surfaces. The three surfaces chosen for testing were the 200 μm in-line (200IL) pattern, 200 μm staggered (200S) pattern, and 25 μm in-line (25IL) pattern.

Tests were conducted in an environmentally controlled room at Kansas State University's IER at ambient conditions of 22 $^{\circ}\text{C}$ and specified RH. This room had uncertainties of ± 1 $^{\circ}\text{C}$ for temperature and $\pm 3\%$ for RH. Figure 5.1 shows maximum freezing temperature for each surface temperature at 30% and 60% RH. Table 5.1 shows the differences in freezing time between all non-hydrophilic surfaces for both 30% and 60% relative humidity. Table 5.2 shows the maximum freezing temperature, number of drops per cm^2 , average drop diameter, standard deviation (STD) of the drop diameter, the percentage of the project area covered with drops, estimated average volume of a drop, and the volume of water per cm^2 , all with their relative uncertainties.

Figure 5.1: Maximum freezing temperature for all surfaces with thermocouple uncertainty

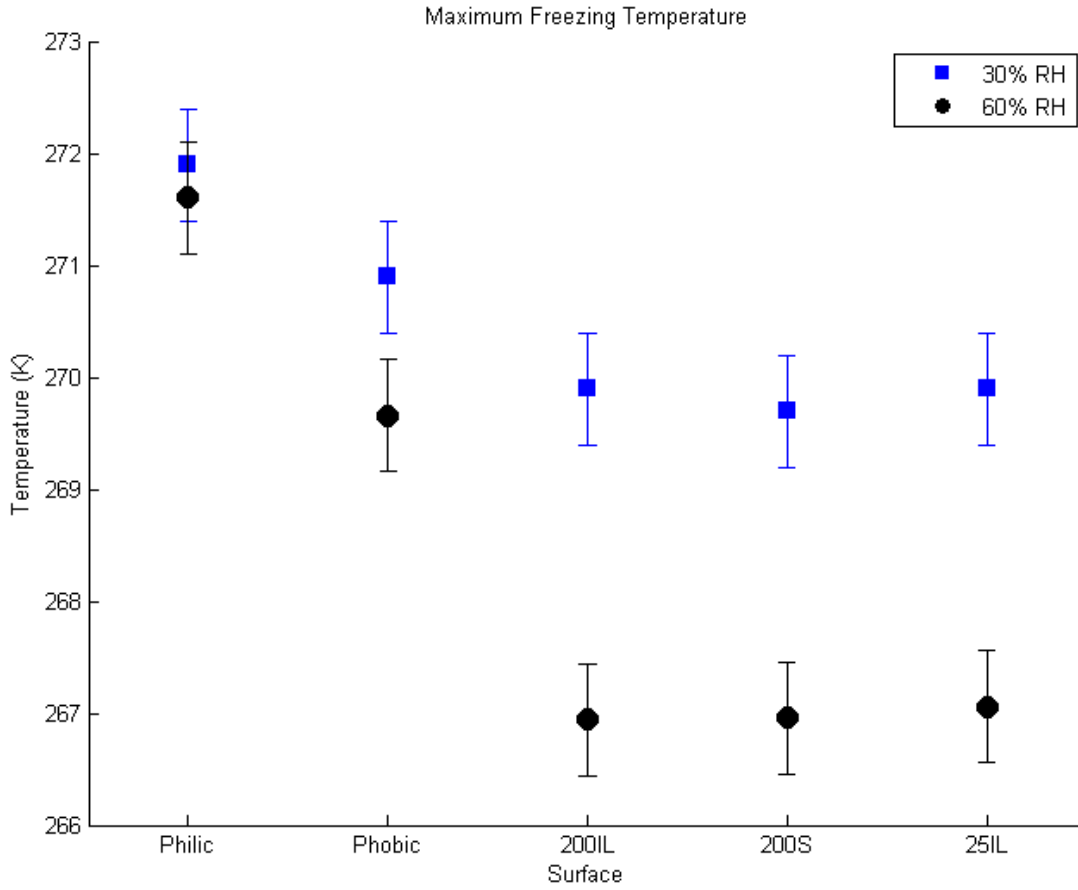


Table 5.1: Freezing time data for 30% and 60% RH for all non-hydrophilic surfaces

Surface	Phobic	200IL	200S	25IL
Freezing time (min:sec) ± 1 second (30% RH)	56:00	37:00	48:00	30:00
Freezing time (min:sec) ± 1 second (60% RH)	25:30	37:15	28:00	32:45

Table 5.2: Average data for 60% RH frozen droplets for all non-hydrophilic surfaces

Surface	Phobic	200IL	200S	25IL
Freezing time (min:sec) ± 1 second	25:30	37:15	28:00	32:45
Maximum freezing temp (K) ± 0.5 K	269.7	266.9	267.0	267.1
Number of drops per cm^2	326 \pm 10	239 \pm 14	618 \pm 35	305 \pm 32
Average drop diameter (mm)	0.55	0.57	0.43	0.45
STD of drop diameter (mm)	.153	.131	.057	.099
% projected area covered with drops $\pm 2.5\%$	62.2	63	90.9	50.5
Estimated average volume of a drop (nL)	48.98	75.17	29.85	37.45
Volume of water per cm^2 ($\mu\text{L}/\text{cm}^2$)	15.97	17.97	18.45	11.42

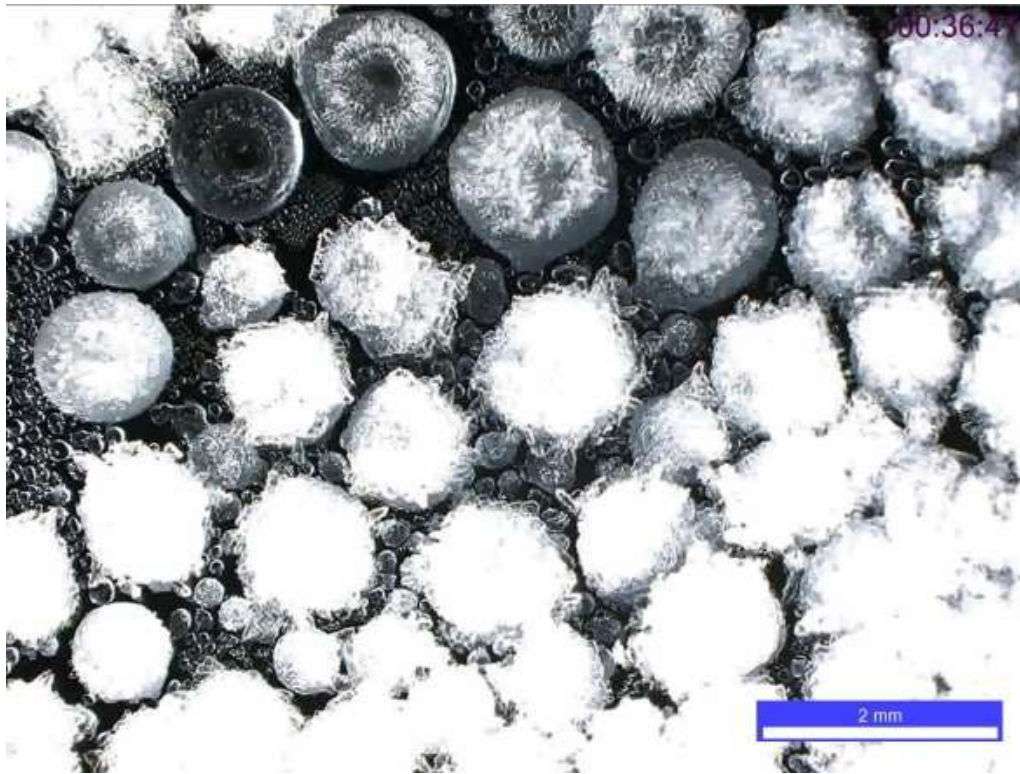
To find the number of drop values in Table 5.2, frozen droplets for each surface were counted by three random people from a pool of five people in one of four randomized quadrants of the images from Figure 5.4 below. The projected area was determined by taking the measured diameter of every drop in the quadrant and finding the area this diameter covers. These values are then averaged and multiplied by the number of drops in a cm^2 . The estimate average volume of a drop was calculated from every measure diameter. It assumes a contact angle of 105° and no coalesced droplets. The total volume of water was determined by multiplying the average droplet volume by the total number of drops in a cm^2 . Due to the small number of individuals taking measurements of the droplets, the uncertainty of the number of drops is half of the range of the counted values.

The 25IL surface was also tested at 75% RH. Figure 5.2 shows the difference in the freezing states for 30%, 60%, and 75% RH. This shows the major differences between condensation nucleation for these three different humidities. Between each humidity change, there is a significant increase in droplet size and decrease in droplet count.

Figure 5.2: Freezing on the 25IL surface at (a) 30%, (b) 60%, and (c) 75% RH

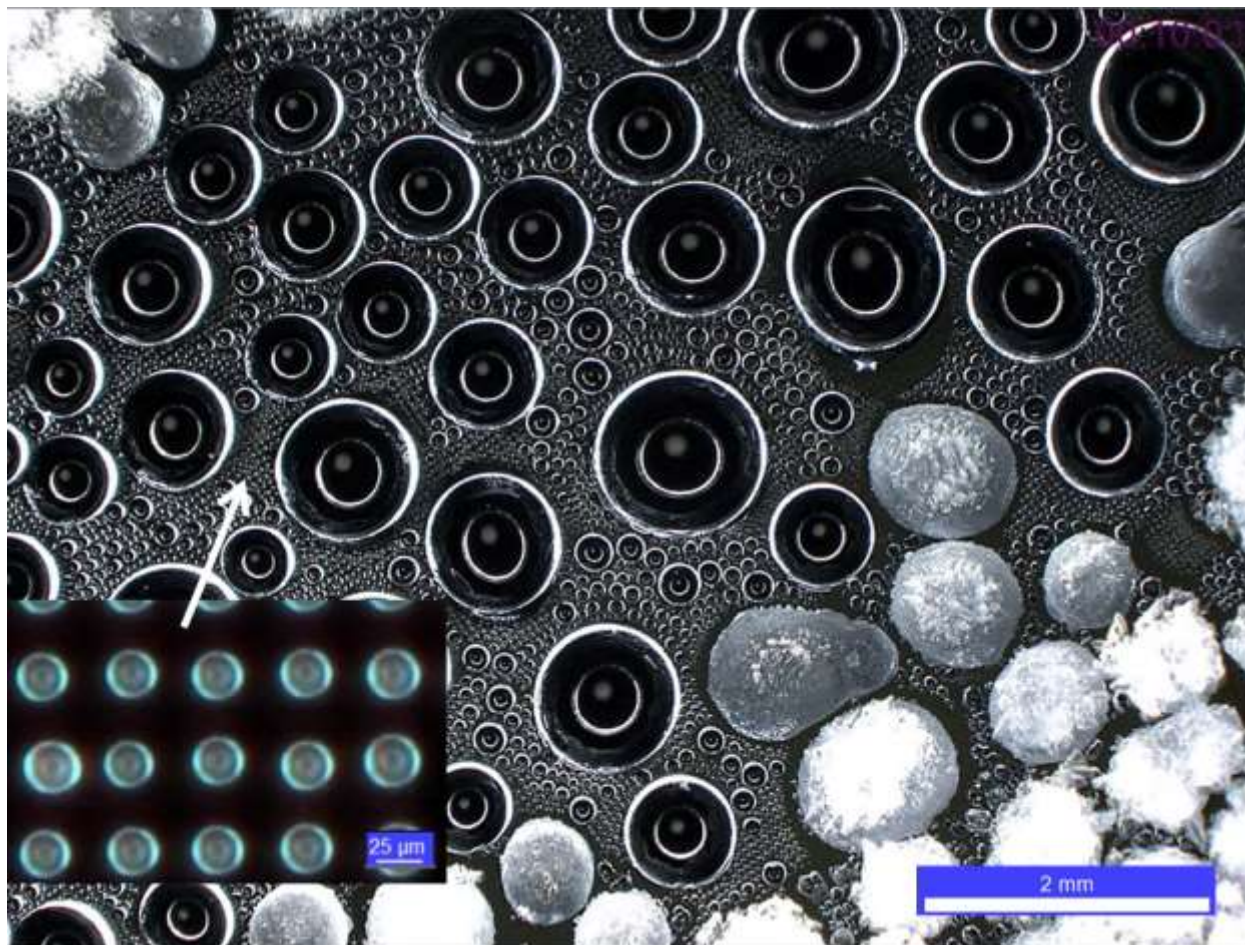


(c)



It was observed that the 75% RH has, by far, the largest droplets of the three. Also, many more of the droplets at 75% RH explosively froze, affecting the neighboring droplets and causing them to freeze. During the nucleation and growth process on the 25IL surface, the nucleation in the pattern continues to grow until contacting neighboring nucleation droplets, then coalescing with those to form larger droplets. Figure 5.3 shows the nucleation in the pattern of the surface as well as the large droplets that the nucleation grows into.

Figure 5.3: Nucleation and coalescence on the 25IL surface at 75% RH



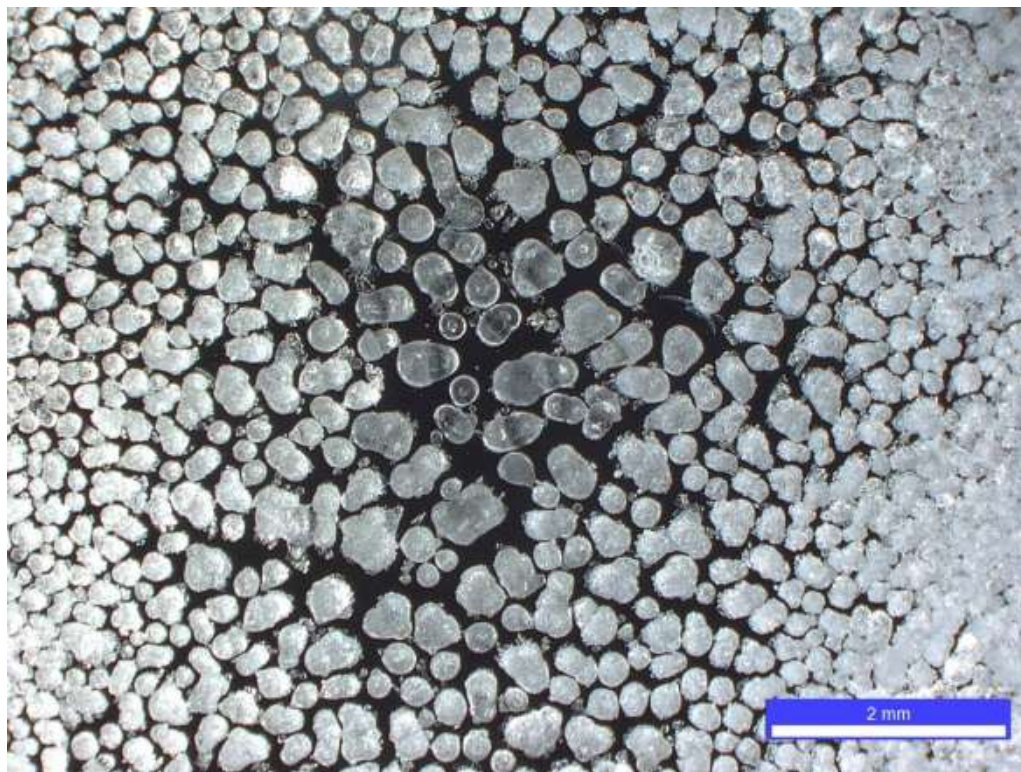
5.2 Discussion

Results indicated that biphilic surfaces depress condensation freezing temperature to colder temperatures than plain hydrophobic surfaces. No discernable difference in biphilic pattern size or orientation was observed for the freezing temperature. However, there is a significant difference between the freezing time and the volume of water, as seen in Table 5.1. From Figure 5.1, freezing at 30% RH occurred at a higher temperature because droplet size at freezing was smaller than droplets at 60% RH. Even though the drops were smaller, there were so many more of them that the freezing time was longer for the 30% RH when compared to the 60% RH. Figure 5.4 shows droplet sizes at nucleation and freezing for both RHs on all surfaces except the hydrophilic surface because the hydrophilic surface freezes in a sheet. The fundamental understanding gained in this study is that the difference in nucleation is the mechanism for the

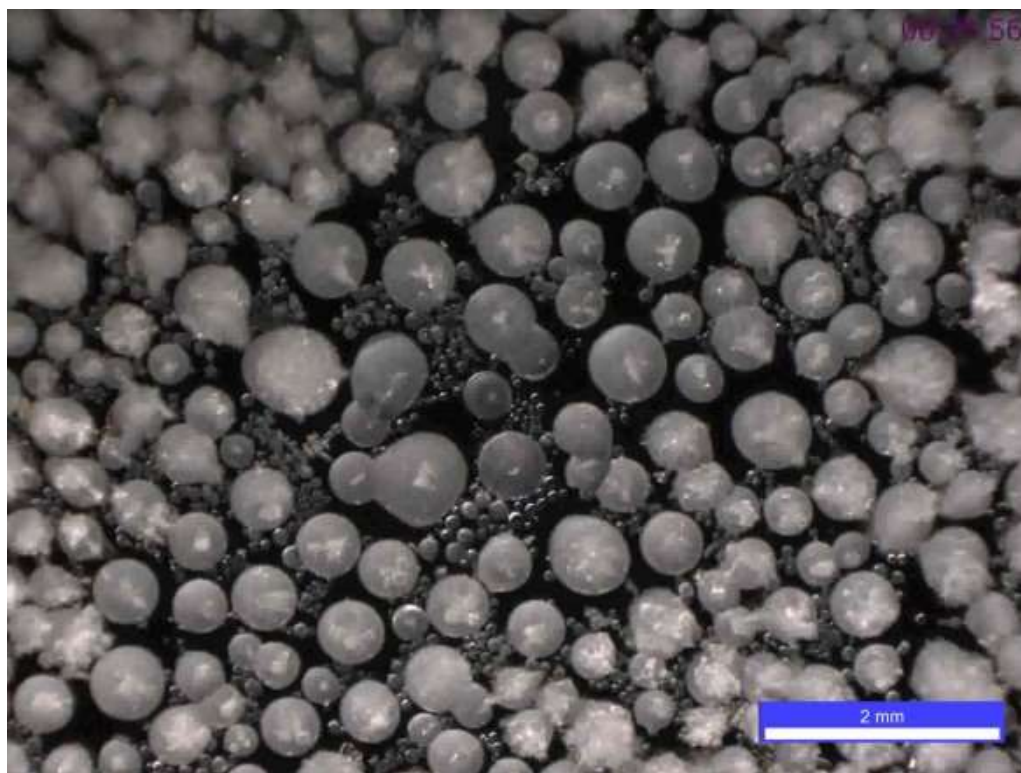
different behavior in coalescence, while the different behavior in coalescence is the mechanism for the difference in freezing behavior.

Figure 5.4: Freezing droplets at (30%, 60%) RH for the (a, b) hydrophobic surface, (c, d) 200IL surface, (e, f) 200S surface, and (g, h) 25IL surface

(a)



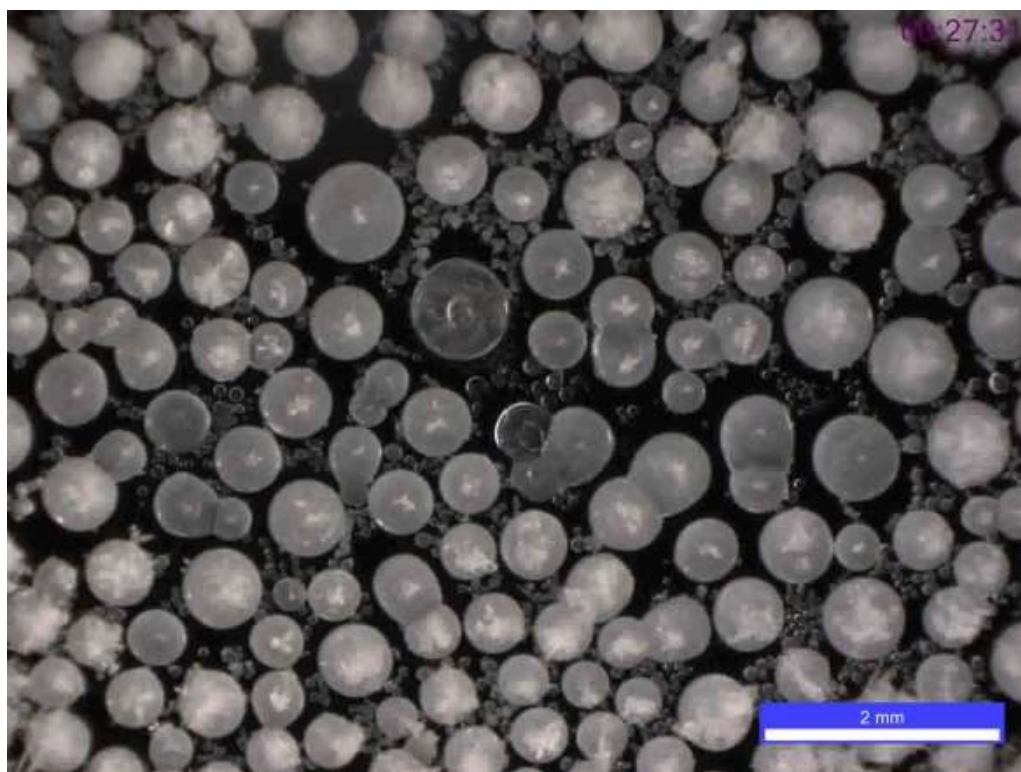
(b)



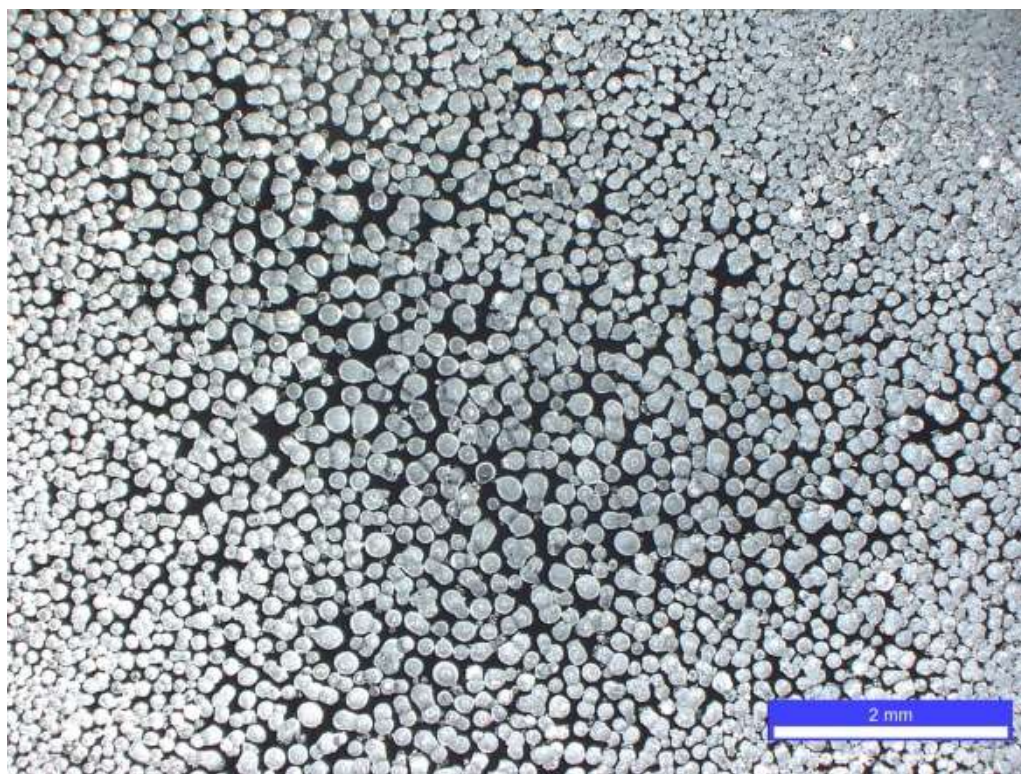
(c)



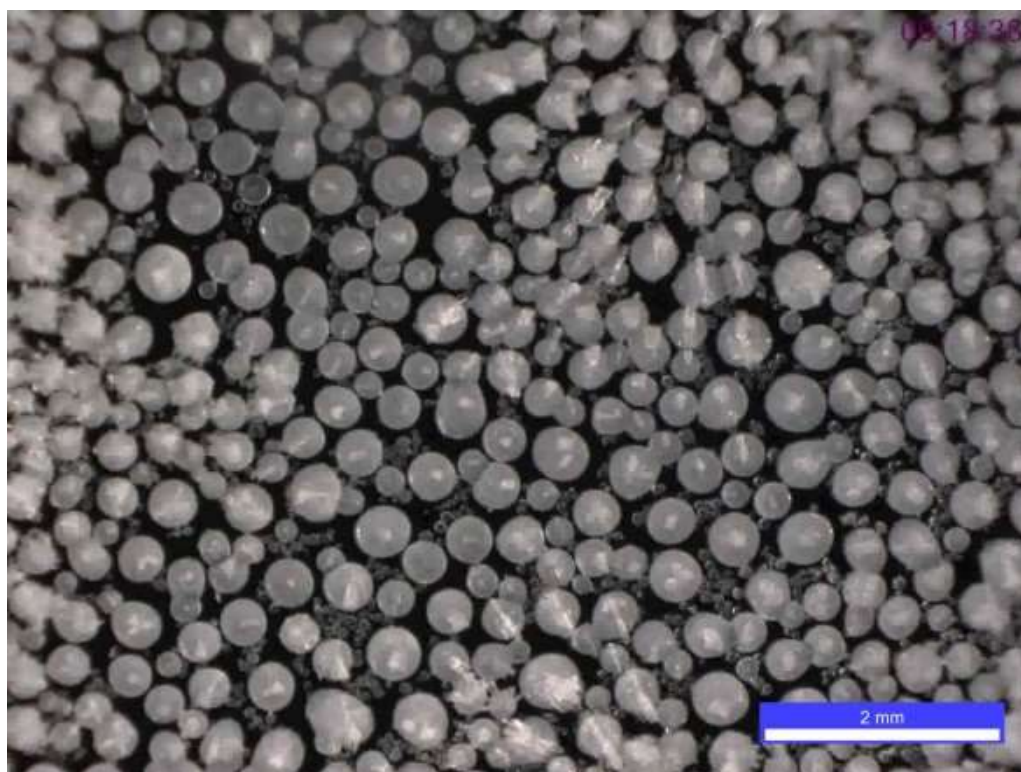
(d)



(e)



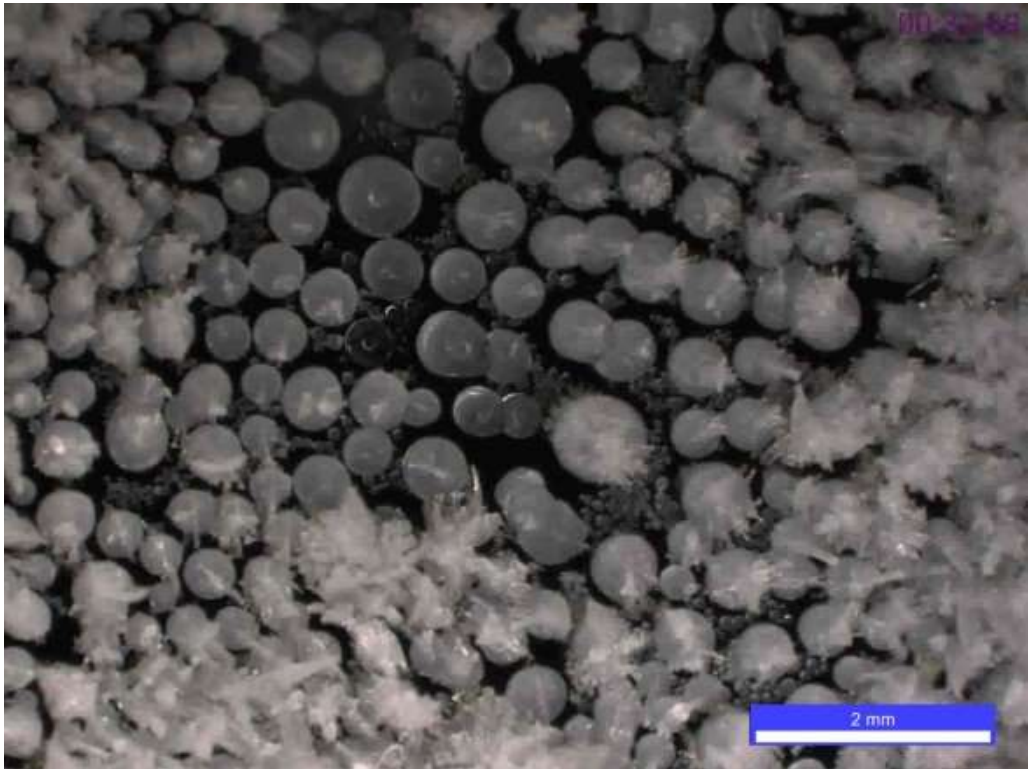
(f)



(g)

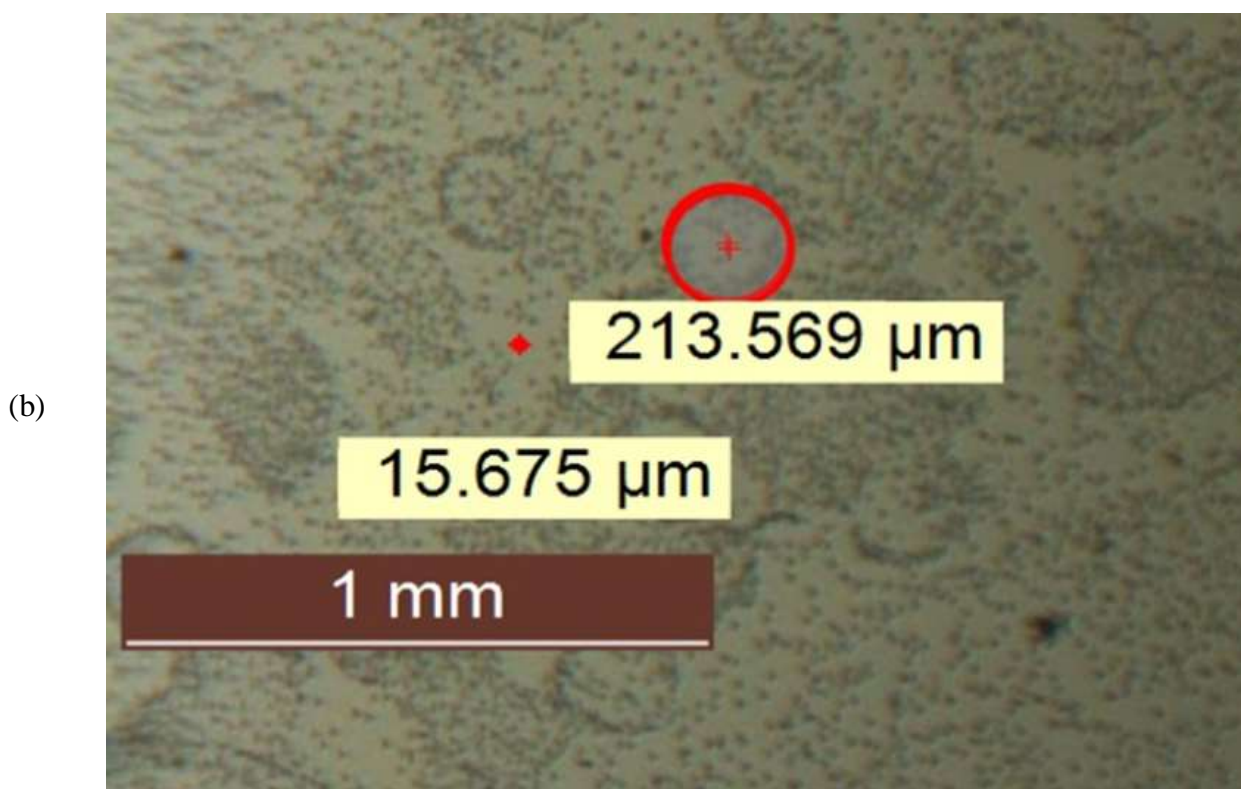
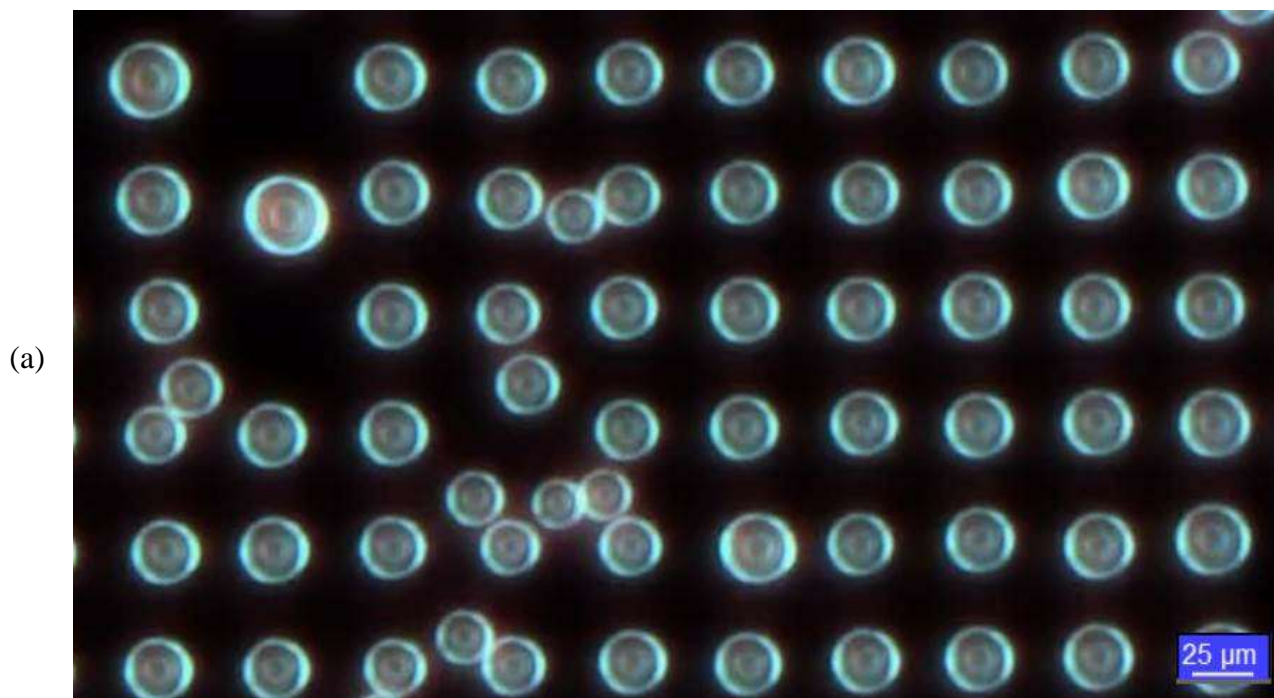


(h)



During nucleation on the 200IL biphilic surface, an expected increased concentration of condensation droplets occurred inside the hydrophilic areas due to the low hydrophilic Gibbs free energy barrier to nucleation. Theory supports the idea that a biphilic surface pins nucleation to designated areas [40, 42-43]. This pinning phenomenon was not observed when the 200IL biphilic surface was tested because the feature size was an order of magnitude larger than the nucleation. However, there was a concentration of nucleation around the pattern on the 200IL surface, shown in Figure 5.5, which shows that nucleation behavior is still affected by the surface modification. Tests of the 25IL biphilic surface supported the theory because pinning did occur on this surface, but pinning was constrained to the pattern, as shown in Figure 5.5, in which the entire surface exhibited areas of missing condensation and areas of condensation between patterns.

Figure 5.5: (a) Pinning of water nucleation on the 25IL biphilic surface, (b) accumulation of nucleation at pattern interface, but no pinning on the 200S biphilic surface



Further testing will include biphilic surfaces ranging from 5 μm features to 200 μm features. Testing will also be conducted at 75% RH for all surfaces. A fractal pattern will be fabricated to maximize pattern density on the surface, which is assumed to contribute to improvements in freezing delay. These tests will be conducted at constant temperature using a freezing stage. Once a suitable method of measuring density was decided upon, density will be analyzed and compared to previous results [10]. Future work will also include using MATLAB so that images and videos may be analyzed to ensure accuracy of times and measurements. A mathematical model of frost growth under varying conditions and homogeneous and heterogeneous wettability surfaces will be developed.

References

- [1] N.T. Nguyen and S.T. Vereley. “Fundamentals and Applications of Microfluidics”, Artech House, Norwood, MA, 2002.
- [2] R. O. Piucco, C. J. L. Hermes, C. Melo, and J. R. Barbosa Jr. A study of frost nucleation on flat surfaces. *Experimental Thermal and Fluid Science*, 2008, 32, pp. 1710-1715.
- [3] J. Irragorry, Y.X. Tao, and S. Jia. Review Article: A Critical Review of Properties and Models for Frost Formation Analysis. *HVAC&R Research*, 2014, 10, pp. 393-420.
- [4] S. Jung, M. K. Tiwari, N. V. Doan, and D. Poulikakos. Mechanism of supercooled droplet freezing on surfaces. *Nature Communications*, 2012, 3, p. 615.
- [5] K. K. Varanasi, T. Deng, J. D. Smith, M. Hsu, and N. Bhate. Frost formation and ice adhesion on superhydrophobic surfaces. *Applied Physics Letters*, 2010, 97.
- [6] A. A. Lambregts, G. Nesemeier, J. E. Wilborn and R. L. Newman. Airplane upsets: Old problem, new issues. *Presented at AIAA Modeling and Simulation Technologies Conference and Exhibit*. 2008.
- [7] L. L. Cao, A. K. Jones, V. K. Sikka, J. Z. Wu, and D. Gao. Anti-Icing Superhydrophobic Coatings. *Langmuir*, 2009, 25, pp. 12444-12448.
- [8] Z. G. Guo, W. M. Liu, and B. L. Su, Superhydrophobic surfaces: From natural to biomimetic to functional. *Journal of Colloid and Interface Science*, 2011, 353, pp. 335-355.
- [9] M. He, J. X. Wang, H. L. Li, X. L. Jin, J. J. Wang, B. Q. Liu, and Y. L. Song. Superhydrophobic film retards frost formation. *Soft Matter*, 2010, 6, pp. 2396-2399.
- [10] S. Jung, M. Dorrestijn, D. Raps, A. Das, C. M. Megaridis, and D. Poulikakos. Are superhydrophobic surfaces best for icephobicity? *Langmuir*, 2011, 27, pp. 3059-3066.
- [11] L. Oberli, D. Caruso, C. Hall, M. Fabretto, P. Murphy, and D. Evans. Condensation and freezing of droplets on superhydrophobic surfaces. *Adv. Colloid Interface Sci.* 2014, 210 pp. 47-57.
- [12] J. B. Boreyko and C. P. Collier. Delayed frost growth on jumping-drop superhydrophobic surfaces. *ACS Nano*, 2013, 7(2), pp. 1618-1627.
- [13] Y. Sohn, D. Kim, S. Lee, M. Yin, J. Song, W. Hwang, S. Park, H. Kim, Y. Ko, and I. Han. Anti-frost coatings containing carbon nanotube composite with reliable thermal cyclic property. *Journal of Materials Chemistry A: Materials for Energy and Sustainability*, 2014, 2(29), pp. 11465-11471.

- [14] T. Jing, Y. Kim, S. Lee, D. Kim, J. Kim, and W. Hwang. Frosting and defrosting on rigid superhydrophobic surface. *Appl. Surf. Sci.* 2013, 276, pp. 37-42.
- [15] P. Kim, T. - Wong, J. Alvarenga, M. J. Kreder, W. E. Adorno-Martinez, and J. Aizenberg. Liquid-infused nanostructured surfaces with extreme anti-ice and anti-frost performance. *ACS Nano* 2012, 6(8), pp. 6569-6577.
- [16] S. Garimella. Innovations in energy efficient and environmentally friendly space-conditioning systems. *Energy*, 2003, 28(15), pp. 1593-1614.
- [17] S. Padhmanabhan, D. E. Fisher, L. Cremaschi, and J. Knight. Comparison of frost and defrost performance between microchannel coil and fin-and-tube coil for heat pump systems. *Presented at 12th International Refrigeration and Air Conditioning Conference at Purdue*, West Lafayette, IN, 2008.
- [18] S. N. Kondepudi and D. L. O'Neal. Effect of frost growth on the performance of louvered finned tube heat exchangers. *Int. J. Refrig.* 1989, 12(3), pp. 151-158.
- [19] K. -. Lee. A one-dimensional model for frost formation on a cold flat surface. *Int. J. Heat Mass Transfer* 1997, 40(18), pp. 4359-4365.
- [20] B. Na, R.L. Webb. A fundamental understanding of factors affecting frost nucleation. *Int. J. Heat Mass Transfer* 46 (2004) 3797–3808.
- [21] J. Shin, A. Tikhonov, and C. Kim. Experimental study on frost structure on surfaces with different hydrophilicity: Density and thermal conductivity. *Journal of Heat Transfer* 2003, 125(1), pp. 84-94.
- [22] Y. Xia, Y. Zhong, P. S. Hrnjak and A. M. Jacobi. Frost, defrost, and refrost and its impact on the air-side thermal-hydraulic performance of louvered-fin, flat-tube heat exchangers. *Int. J. Refrig.* 29(7), pp. 1066-1079. 2006.
- [23] N.H. Fletcher, 1970, “The chemical physics of ice”, Cambridge University Press, Cambridge, UK.
- [24] D. Attinger, C. Frankiewicz, A.R. Betz, T.M. Schutzius, R. Ganguly, A. Das, C.J. Kim, and C.M. Megaridis. Surface Engineering for Phase Change Heat Transfer: A Review. *MRS Energy & Sustainability*, 2014, 1(4).

- [25] A. Van Dyke and A. R. Betz, .The effect of mixed hydrophilic and hydrophobic surfaces on frost nucleation and growth. *Presented at ASME International Mechanical Engineering Congress and Exposition*, San Diego, CA, 2013.
- [26] R. Becker and W. Döring. Kinetische Behandlung der Keimbildung in übersättigten Dämpfen. *Ann. Phys (Leipzig)*., 1935, 24, pp 719-752.
- [27] Hayashi, Y., A. Aoki, S. Adachi, and K. Hori. Study of Frost Properties Correlating With Frost Formation Types. *Journal of Heat Transfer*, 1977, 99, pp. 239-245.
- [28] M. He, J. Wang, H. Li and Y. Song. Super-hydrophobic surfaces to condensed micro-droplets at temperatures below the freezing point retard ice/frost formation. *Soft Matter*, 2011, 7(8), pp. 3993-4000.
- [29] S. Jung, M.K. Tiwari, and D. Poulikakos. Frost Halos from Supercooled Water Droplets. *PNAS*, 109 (40), pp 16073-16078.
- [30] E. Moallem, S. Padhmanabhan, D. E. Fisher and L. Cremaschi. Experimental study of onset and growth of frost on outdoor coils of air-source heat pump systems. *Presented at ASME-ATI-UTI Conference of Thermal and Environmental Issues in Energy Systems*, Sorrento, Italy, 2010, pp. 1313.
- [31] E. Moallem, L. Cremaschi, D. Fisher and S. Padhmanabhan. Experimental measurements of the surface coating and water retention effects on frosting performance of microchannel heat exchangers for heat pump systems. *Exp. Therm. Fluid Sci.* 2012, 39, pp. 176-188.
- [32] T. Hong, E. Moallem, L. Cremaschi, and D. E. Fisher. Measurements of frost growth on louvered folded fins of microchannel heat exchangers, part:1 experimental methodology. *Presented at ASHRAE Winter Conference*, Chicago, IL, 2012.
- [33] E. Moallem, S. Padhmanabhan, L. Cremaschi, and D. Fisher. Experimental investigation of the surface temperature and water retention effects on the frosting performance of a compact microchannel heat exchanger for heat pump systems. *Int. J. Refrig.* 2012, 35(1), pp. 171-186.
- [34] E. Moallem, T. Hong, L. Cremaschi and D. Fisher. Experimental investigation of adverse effect of frost formation on microchannel evaporators, part 1: Effect of fin geometry and environmental effects. *Int. J. Refrig.* 2013, 36(6), pp. 1762-1775.

- [35] E. Moallem, T. Hong, L. Cremaschi and D. E. Fisher. Effects of surface coating and water retention of frost formation in microchannel evaporators (AHSRAE RP-1589). *HVAC and Refrigeration Research*, 2013, 19, pp. 779.
- [36] E. Moallem, T. Hong, L. Cremaschi and D. E. Fisher. Developing empirical correlations for frost thickness and air face velocity degradation for microchannel heat exchangers used in heat pump applications under frosting conditions. *HVAC and R Research* 19(7), pp. 779-787. 2013.
- [37] E. Moallem, S. Padhmanabhan, D. E. Fisher and L. Cremaschi. Experimental study of onset and growth of frost on outdoor coils of air-source heat pump systems. *Presented at ASME-ATI-UTI Conference on Thermal and Environmental Issues in Energy Systems*, Sorrento, Italy, 2010.
- [38] L. Zhai, M.C. Berg, F.C. Cebeci, Y. Kim, J.M. Milwid, M.F. Rubner, and R.E. Cohen. Patterned Superhydrophobic Surfaces: Toward a Synthetic Mimic of the Namib Desert Beetle. *NANO Letters*. 2006, 6 (6), pp1213-1217.
- [39] T. Maitra, M. K. Tiwari, C. Antonini, P. Schoch, S. Jung, P. Eberle, and D. Poulikakos. On the Nanoengineering of Superhydrophobic and Impalement Resistant Surface Textures below the Freezing Temperature. *Nano Lett.*, 2014, 14 (1), pp 172–182.
- [40] P. Eberle, M.K. Tiwari, T. Maitra, and D. Poulikakos. Rational Nanostructuring of Surfaces for Extraordinary Icephobicity. *Nanoscale*, 2014, 6, pp4874-4881.
- [41] K. Rykaczewski, S. Anand, S. B. Subramanyam, and K.K. Varanasi. Mechanism of Frost Formation on Lubricant-Impregnated Surfaces. *Langmuir*, 2013, 29 (17), pp 5230-5238.
- [42] A.R. Betz, J. Xu, H. Qiu, and D. Attinger. Do Surfaces with Mixed Hydrophilic and Hydrophobic Areas Enhance Pool Boiling? *Applied Physics Letters*, 2010, 97, 141909-1-141909-3.
- [43] Jhee, Sung, Kwan-Soo Lee, and Woo-Seung Kim. Effect of Surface Treatments on the Frosting/Defrosting Behavior of a Fin-tube Heat Exchanger. *Int. J. Refrigeration*, 2002, 25 (8), pp 1047-1053.